A COMPREHENSIVE STUDY OF THE EAGLE FORD SHALE FRACTURE CONDUCTIVITY

A Thesis

by

OMAR ENRIQUEZ TENORIO

Submitted to the Office of Graduate and Professional Studies of
Texas A&M University
in partial fulfillment of the requirements for the degree of

MASTER OF SCIENCE

Chair of Committee,	Ding Zhu
Committee Members,	A. Daniel Hill
	Michael Pope
Head of Department,	A. Daniel Hill

August 2016

Major Subject: Petroleum Engineering

ABSTRACT

The aim of this study was to develop an understanding of the Eagle Ford shale unpropped and propped fracture conductivity. Samples were collected at Antonio Creek and Lozier Canyon. Both outcrops are several hundred feet thick and extend for a few thousand feet laterally. At these locations five different geological facies (A, B, C, D and E), each with distinct lithological characteristics and geochemical properties that can be correlated to the Eagle Ford shale in the subsurface are accessible. The mineralogy of the collected samples was determined via x-ray diffraction which corroborates the relationship of the samples to the outcrops and hence to the Eagle Ford shale in the subsurface.

After collected, the samples were cut into modify API conductivity cell dimensions. The fracture conductivity at different closure stresses was determined based on laboratory measurements of flow rate and pressure drops along the fracture. The fluid used in this work was nitrogen. The proppant concentration used is representative of what is commonly used in hydraulic fracturing treatments in the Eagle Ford shale. The heterogeneity of the Eagle Ford shale is addressed by obtaining conductivity samples in two different directions with respect to the bedding plane for the five geological facies. Three directions were obtained for facies B.

Fracture area and fracture roughness (surface attributes) were calculated from the data taken by a surface profilometer. The mechanical properties, namely Young's modulus, Poisson's ratio and Brinell hardness, were experimentally determined from core plugs acquired from the same rocks where the conductivity samples were obtained. The

effect that the surfaces attributes, mechanical properties and geological facies (mineralogy) have on conductivity was analyzed and the major findings of this work are the following.

From this study, we found that fracture orientation has an impact on the fracture conductivity. It was also found that the geological characteristics (mineralogy) and mechanical properties (Poisson's Ratio) impact the fracture conductivity. The geological facies (lithology) impact the fracture conductivity in Eagle Ford shale. Facies A, B and C exhibit a good relationship between fracture conductivity and surface attributes (fracture roughness and area). This relationship is not present in facies D and E.

This work provides a foundation for future studies (damage mechanism) of the Eagle Ford shale fracture conductivity and gives an insight into the relationship of fracture conductivity and geological facies.

DEDICATION

I would like to dedicate this work to my family: My wife Sarah Henry, my parents Roberto Enriquez and Paola Tenorio, my siblings Edgar Enriquez and Paola Enriquez and to the rest of my family. Even though you may not know exactly what I am up to, I have always felt your unconditional support.

ACKNOWLEDGEMENTS

I would like to express my sincere gratitude to both Dr. Ding Zhu and Dr. Daniel Hill for giving the opportunity to join the fracture conductivity research group. The discussions and conversations that we have during weekly meeting and during individual meetings definitely enhance my professional development as well as my personal development. I would like to especially thank Dr. Zhu, for helping me to make the decision that graduate school was the right path for myself, after completing my studies I am confident that I chose the right path.

I would also like to thank Dr. Michael Pope for serving as a committee member. Next, I would like to thank BP for allowing the collection of samples in Lozier and Antonio creek canyons.

I would like to thank the members of the fracture conductivity research group that I have had the privilege to work with: Bill Foran, Dante Guerra, Cody Kainer, Ashley Knorr, Mark McGinley and Paola Perez. I can certainly say that I have learned something from all of you. I would like to thank Jesse Guerra for developing the code for the surface attributes. I would also like to thank all the previous members of the conductivity group, your work provided a solid foundation to start my own work.

I would like to thank John Maldonado and the rest of the Petroleum Engineering staff for their help during my experiments. Finally, I would like to thank RPSEA for the financial support provided for this work.

NOMENCLATURE

A_{flow}	Cross sectional area of flow, L^2, in^2
$A_{fracture}$	Fracture Area, L^2, in^2
bbl	Barrel of oil, L^3 , 42 US gal
BI	Brittleness index, dimensionless
C_a	Areal proppant concentration, $ML^{-2}, lbm/ft^2$
cf	cubic foot, L^3
C_{fd}	Dimensionless fracture conductivity, dimensionless
C_f	Fracture Conductivity, L^2L, md-ft
d_p	Proppant diameter, L, mm
h_f	Sample width, L, ft
k_f	Fracture Permeability, L^2, md-ft
k_m	Matrix Permeability, L^2, md-ft
L	Sample length, L, ft
$\dot{m}$	Mass flow rate, Mt^{-1}, kg/min
M_g	Molecular Mass, $MM^{-1}N^{-1}$, Kg/Kg mol
M	One thousand, dimensionless
MM	One Million, dimensionless
P_{cell}	Cell pressure, $ML^{-1}r^2$, psig
P_2	Downstream pressure, $ML^{-1}r^2$, psig

Ppg	Pounds per gallon, ML^{-3}, lbm/gal
P_1	Upstream pressure, $ML^{-1}r^2$, psig
q	Volumetric flow rate, L^3t^{-1}, L/min
R	Universal gas constant, $ML^2t^{-2}N^{-1}\varphi^{-1}$, J/mol-K
T	Temperature, K
w_f	Fracture width, L, in
v	Fluid velocity, Lt^{-1}, ft/s
x_f	Fracture half length, L, ft
Z	Gas compressibility factor, dimensionless

Greek

γ_p	Proppant specific gravity, dimensionless
$\emptyset$	Porosity, fraction
μ	Fluid viscosity, $ML^{-1}T^{-2}T$, Pa-s
ΔP	Differential pressure, $ML^{-1}r^2$, psig
ρ_f	Fluid density, ML^{-3}, lbm/ft^3

TABLE OF CONTENTS

Page

LIST OF FIGURES

Page

LIST OF TABLES

Page

1. INTRODUCTION

1.1 Background

Hydraulic fracturing is a stimulation process that involves pumping a pressurized mixture of fluids, chemicals and proppants (usually sand) down a well. On high permeability reservoirs the objective of hydraulic fracturing is to bypass a damage zone near the wellbore. On the other hand, in low permeability formations like shale reservoirs the objective is to increase the contact area with the reservoir so commercial flow rates can be obtained. The hydraulic fracturing process begins with pumping pad fluid at pressures higher than the formation fracturing pressure which fractures the rock. Next, proppants are added to the fluids and it is expected that the proppants will fill the newly created fractures and keep them open once the pumping stage is over. Chemicals are added at every stage of the hydraulic fracturing process. These chemicals are used to reduce the friction between the slurry and the pipe, increase and maintain the fluid viscosity, limit corrosion and scale deposition in the pipe, clean the perforations and to avoid/minimize formation damage.

Unconventional reservoirs, specifically shale reservoirs, are heterogeneous as can be seen from the wide range of productions that are observed from the same formation. For example, the Eagle Ford shale produces dry gas on its eastern regions and black oil on its western region. Production rates and fluid characteristics from wells located in the same region can be very different. Therefore understanding the impact that reservoir heterogeneity has on the fracture conductivity is essential to understand shale reservoirs.

With this in mind we performed a systematic investigation of the fracture conductivity of multiple lithological facies presented in the Eagle Ford shale.

1.2 Literature Review

In this section a literature review of the fracture conductivity, its controlling parameters, the Eagle Ford shale and its importance are presented.

1.2.1 Hydraulic Fracturing of Unconventional Reservoirs-Eagle Ford Shale

The first experiments of the oil and gas industry with hydraulic fracturing were performed more than sixty years ago. By 1950 the process was commercialized and horizontal wells were common by the late 1970s (King 2012). Modern hydraulic fracturing treatment can be traced back to the development of the Barnett shale by Mitchell Energy. After experimenting with multiple stimulation techniques, Mitchell Energy found success by combining vertical wells with hydraulic fracturing in the late 1990s. A few years later the development of the Barnett shale was evident and is illustrated by the natural gas production rate that went from 216 MMcf per day in 2000 to 3,045 MMcf per day in 2007 (RRC 2016a). The lessons and techniques learned in the Barnett shale were used in other unconventional plays like the Bakken, Eagle Ford, Haynesville, Marcellus, Niobrara, Permian and Utica. These plays accounted for more than ninety percent of the domestic oil and gas production growth between 2011 and 2014 and in 2015 produce 4 MMbbl of oil per day and more than 44,127 MMcf of natural gas per day (EIA 2016).

The first well to obtain commercial production from the Eagle Ford shale was drilled in 2008 by Petrohawk, now a part of BHP Billiton. The well was drilled in La Salle County and flowed at 7.6 MMcf of natural gas per day from a 3,299 ft lateral well with 10 hydraulic fracturing stages. After the discovery of the play the interest and activity increased. In 2008 there were 26 drilling permits for the Eagle Ford shale and in 2014 there were 5,613 drilling permits. Amid the recent decrease in hydrocarbon prices in 2015 there were 2,315 new drilling permits. Production went from less than 500 bbl of oil in 2008 to more than a million barrels of oil in 2015 (January-November data for 2015). In the same manner gas production went from 2 MMcf in 2008 to 5,366 MMcf in 2015 (January-November data for 2015) (**Fig. 1.1**).

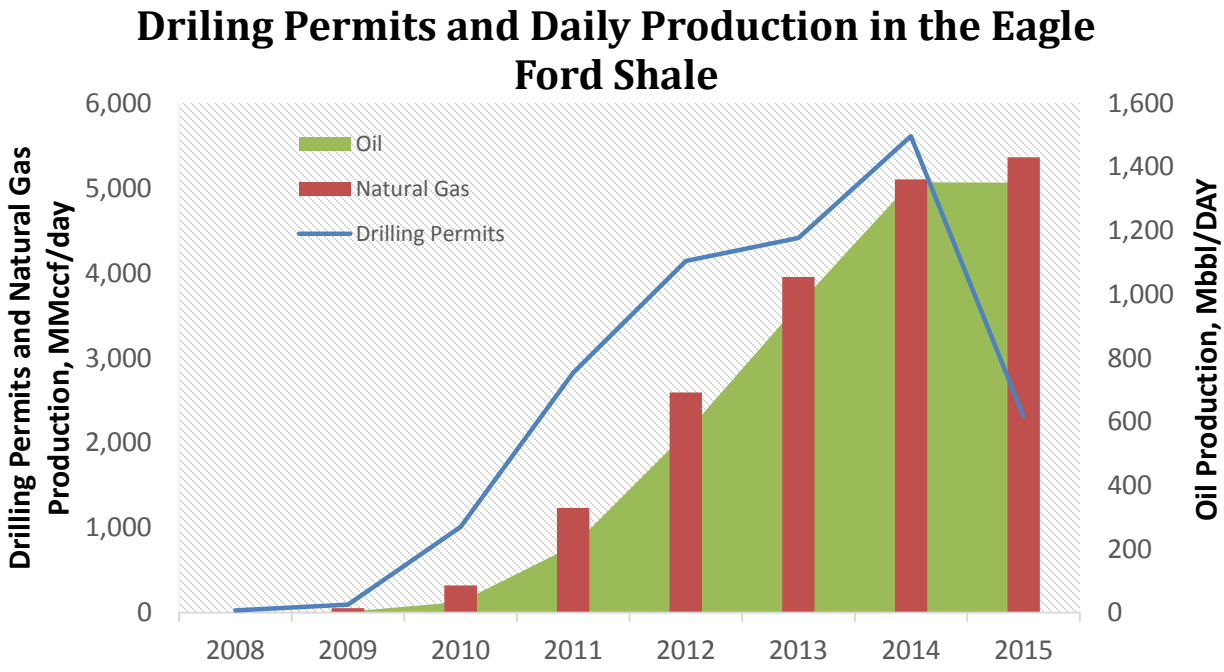

Fig. 1.1 – Drilling Permits and Average Daily Oil and Gas Production in the Eagle Ford Shale (RRC 2016b).

1.2.2 Fracture Conductivity

Fracture conductivity (C_f) is defined as the product of fracture permeability (k_f) and fracture width (w_f). Fracture conductivity, **Eq. 1-1**, can be calculated by combining well testing analysis with production data and also by laboratory experiments,

$$C_f = k_f w_f \quad \text{(1-1)}$$

Cinco-Ley et al (1978) developed a mathematical model to correlate well production via an equivalent skin factor (s_f) created by the hydraulic fracturing to the dimensionless fracture conductivity (C_{fd}) which is defined by **Eq. 1-2**. A graphical interpretation of this relationship is shown in **Fig. 1.2**.

$$C_{fd} = \frac{k_f w_f}{k_m x_f} \quad \text{(1-2)}$$

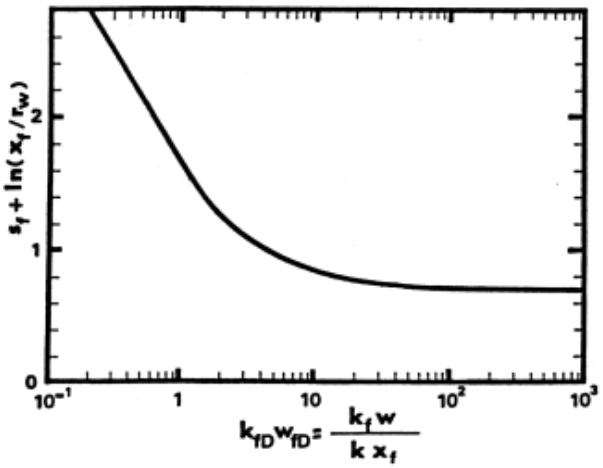

Fig. 1.2 –Equivalent Skin Factor, Fracture Half Length and Dimensionless Fracture Conductivity (Cinco-Ley et al. 1978).

Where x_f is the fracture half length; k_f is the fracture permeability; w_f is the fracture width and k_m is the reservoir permeability. If fracture half-length and production data are known the fracture conductivity can be calculated from this model. The model was developed for an isotropic homogenous reservoir bounded by two impermeable zones. The model assumes the reservoir fluids are slightly compressible and with constant properties. Fluids are produced through a vertically fractured well.

Determination of fracture conductivity via laboratory experiments has the advantage of controlling and measuring the testing conditions which in turn reduces the unknown variables. The conductivity of a proppant pack in the laboratory is measured following the procedure outlined by ISO 13503-5:2006. This procedure consists of flowing 2% KCL solution thorough a proppant pack loaded between two smooth surfaces, commonly sandstone, and the pressure drop along the flow path is recorded. The process is repeated at multiple closure stresses, each closure stress is maintained for fifty hours. By following this procedures multiple labs can obtain comparable results regarding the quality of the proppants.

There are many variations of modified ISO tests used by the different laboratories. The most common variations are to increase the sample's thickness in order to measure fluid leak off, maintaining the closure stress for relatively short periods and using rough fracture faces (Zhang 2014; Aweloke 2013). Another variation is flowing dry gas, wet gas, fresh water, brines individually or in multiphase flow instead of the 2% KCL brine (Barree et al. 2009; Ramurthy et al. 2011).

1.2.3 Fracture Conductivity Controlling Parameters

Due to complex fracture geometries and proppant settling effects it is likely that the proppants are not distributed uniformly and that the fractures contained in the stimulated area may have no proppant, low concentration of proppants and/or high proppant concentration (Warpinski 2009). It has been reported by multiple authors that fractures with a partial monolayer can have a higher conductivity than fully packed fractures at low closure stress (Brannon et al. 2004; Darin and Huitt 1959; Parker et al. 2005; Zhang. 2014). The explanation for this phenomena is that partial monolayer will have a higher porosity than the packed proppants which will yield a higher flow area. However, the small fracture width will create a high fluid velocity which will increase the non-Darcy effect. This problem will become more severe as closure stress increases and the fracture width reduces as a consequence. Furthermore, the load will concentrate into a few proppants which results on a higher stress per proppant. Brannon et al. 2004 presented **Eq. 1-3** to calculate the required proppant concentration to obtain a full proppant monolayer.

$$C_a = 5.20(1 - \emptyset)\gamma_p d_p \quad \text{(1-3)}$$

Where C_a is the minimum proppant concentration required to obtain a full monolayer in lbm/ft^2; $\emptyset$ is the minimum obtainable porosity of the proppant pack in fraction; γ_p is the proppant specific gravity in g/cm^3 and d_p is the average proppant diameter in inches. Gillard et al. (2010) presented a hydraulic fracturing design that combines a special pumping schedule and fluids additives to create a proppant

configuration composed of proppant pillars and channels (**Fig. 1.3**). Fracture conductivity was measured with a short term conductivity experiment following the API RP 61, 1989 procedure. The conductivities obtained were between 1.5 to 2 orders of magnitude higher than the theoretical maximum that can be obtained with a proppant pack. This new treatment was applied in seven wells in Argentina's La Loma La Lata field, low permeability sandstone field, the results were compared to eight offset wells located in the field that were fractured with a conventional method. The new method produced 53% higher initial production and a 15% increase in projected hydrocarbon recovery.

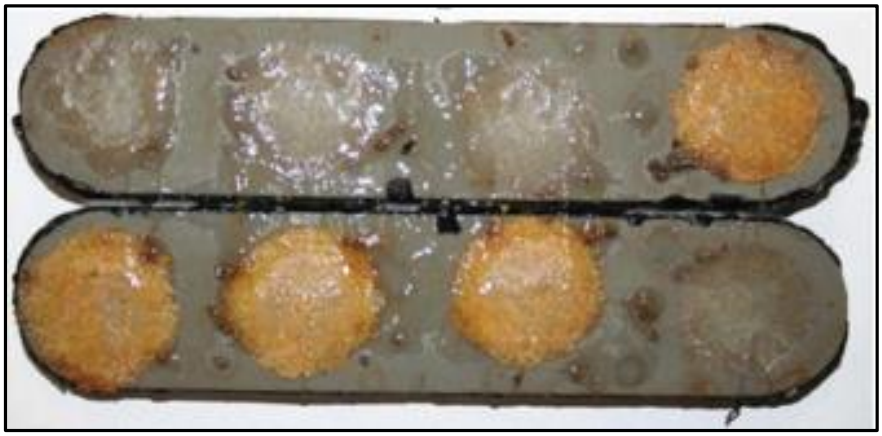

Fig. 1.3 –Proppant Arrangement with Proppant Pillars and Channels on a Fracture Conductivity Sample (Gillard et al. 2010).

Huitt and McGlothlin (1958) performed experiments to determine the embedment of Ottawa sand, 10-12 mesh size, in core samples where embedment is possible. They concluded that embedment of proppant is possible and as a result this diminishes the ability of the formation to maintain a propped fracture. Their equation is valid for

formations where the sands embed completely and no proppant crushing occurs. Kamali and Pournik (2015) developed a mathematical model for rough fractures contact, and then they combined this model with a fluid flow simulator to predict fracture conductivity under different closure stress. They concluded that the conductivity decline depends on the surface profile which dictates the mechanical interaction and deformation of the asperities.

The following studies used nitrogen to calculate fracture conductivity and the proppants were place manually in the fracture surface. Kamenov (2013) executed short term fracture conductivity (propped and unpropped) experiments in Barnett shale outcrop samples. He observed that displaced natural fractures have an order of magnitude higher conductivity than aligned natural fractures due to the contact between two non-matching rough surfaces. He determined that whenever proppant was used, conductivity was proppant dominated and the surface roughness played a smaller role. Zhang (2014) performed fracture conductivity experiments on Fayetteville, Eagle Ford and Barnett outcrops samples. He concluded that fracture conductivity for unpropped samples is well correlated to rock brittleness. By performing fracture conductivity with proppant concentrations lower than 0.15 lbm/ft^2 he demonstrated that low proppant concentrations, including unpropped, have and can maintain fracture conductivities in the 3-30 md-ft range at 4,000 psi closure stress for the Barnett shale outcrop samples. He also observed that when multiple layers of sands were placed in the fracture surface larger sands will have a higher conductivity than smaller sands. When comparing short term (0.5 hours) versus long term conductivity measurements (fifty hours) the short term conductivities

were 20% higher. Briggs (2014) performed short term fracture conductivity in two different zones of the Fayetteville shale. These zones are FL 2 and FL 3. The brittleness and conductivity of zone FL 2 were found to be greater than the ones in FL 3. The results were supported with production data that shows a greater production in FL 2 than in FL 3. Jansen (2014) used the fracture conductivities obtained by Kamenov (2013) and Zhang (2014) and compared these values with the Young's modulus and Poisson's ratio obtained from core plugs. These core plugs were obtained from the same rocks where the conductivities samples were acquired. He concluded that surface roughness dominates the initial conductivity and that the mechanical properties dominate the conductivity decline rate. A higher Young's modulus corresponds to a slower decline rate in conductivity and a higher surface roughness generates a higher initial conductivity. McGinley (2015) tested the propped fracture conductivity of the Marcellus shale (outcrops). He performed his experiments with samples cut in two different directions and concluded that the anisotropy of the mechanical properties decreases the fracture conductivity.

The fracture conductivity calculated at room temperature with nitrogen and without the damage caused by fracturing fluids can be used as a baseline to examine water damage to fracture conductivity. This value has to be decreased in order to take into account all the damage mechanisms. Cooke (1973) concluded that the presence of brine and/or high temperature decreases the fracture conductivity. Cooke (1975) continued his studies of fracture conductivity and concluded that residue from guar polymer, a fracture gelling agent, greatly decreased the fracture conductivity. Davies and Kuiper (1988) demonstrated the importance of multiphase flow and how this condition decreases the

fracture conductivity of each phase. Fine migration, proppant embedment and non-Darcy flow can reduced the fracture conductivity by more than fifty percent (Brannon et al. 2008; Palisch et al. 2007). Awoleke (2013) concluded that an aggressive flow back rate during the cleanup process is a displacement and evaporative process that significantly reduces fracture conductivity. Proppant degradation, which leads to proppant pack porosity reduction as a consequence of chemical reactions, can occur at reservoir conditions over a relatively short period of time (less than a year). This porosity reduction leads to a decrease in fracture permeability and hence a decrease in fracture conductivity (Zheng and Ellsworth 2010; Raysoni and Weaver 2012).

The results from all the authors presented in this section agree that fracture conductivity declines with closure stress. The following list presents a summary of all the factors that affect conductivity and were discussed in this section. This study analyzes the factors presented in numbers 1-6.

1. Mechanical properties: Young's modulus, Poisson's ratio and Brinell hardness
2. Sample orientation
3. Brittleness calculated from the mineralogy
4. Proppant concentration and type
5. Surface attributes: roughness and fracture area
6. Closure stress
7. Embedment
8. Proppant distribution
9. Flow back rate

10. Temperature
11. Long term exposure to stress
12. Multiphase flow and water damage
13. Gel damage

1.2.4 Eagle Ford Depositional Environment and Lithofacies

The Eagle Ford shale play extends from the San Marcos Arch to South Texas into Mexico. It was deposited during the upper cretaceous and overlies the Buda limestone and underlies the Austin Chalk. The Eagle Ford shale is limited on its west flank by uplifting that resulted on an outcrop belt. The shelf margin, formed by the Edwards reef and the Siglo reef trends, marks the eastern boundary of the Eagle Ford. To the north the San Marcos arch marks the division between the Eagle Ford shale and the Eagle Bine. On the south side the Eagle Ford shale extends into Mexico (**Fig. 1.4**). The thickness of this formation decreases in a south to north trend. Maximum thickness of over 600 feet is encountered in the Maverick basin and the minimum thickness of around 50 feet is present near the San Marcos arch.

The formation is commonly divided into the lower Eagle Ford and the Upper Eagle Ford. The lower member contains the highest organic content of the play and is present across the basin. On the other hand, the upper member contains a higher carbonate content and has its maximum thickness in the Maverick basin, southwest region, and thins out towards the San Marcos arch (Martin et al. 2011; Tian et al. 2012). The mineralogy and total organic content show great variation across the play. The dominant mineral is calcite

followed by quartz and clays (Martin et al. 2011; Tian et al. 2012). The total organic content depends on the depositional environment as well as on the maturation. There is not a well-defined trend in this parameter across the play and it seems to be dominated by regional geology and fluid maturation (**Fig. 1.5**).

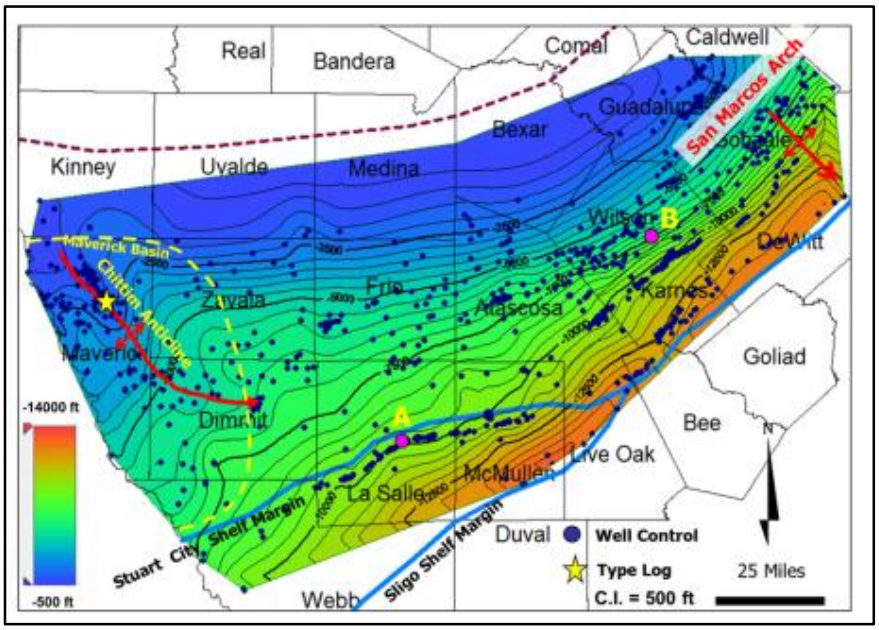

Fig. 1.4 – Major Structural Features of Eagle Ford Shale (Tian et al. 2012).

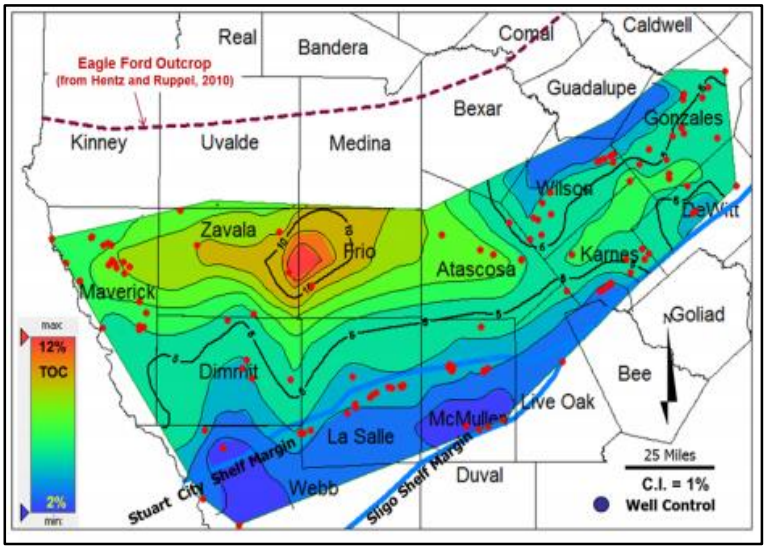

Fig. 1.5 – Total Organic Content of the Lower Eagle Ford Shale Calculated from Sonic and Resistivity Logs (Tian et al. 2013).

More than 500 well logs were analyzed by Tian et al. (2012) and Tian et al. (2013) in order to generate the previous two maps.

1.3 Problem Description, Objectives and Significance

It is accepted by the industry that well production in shale reservoirs is directly related to fracture conductivity. Most of the published data for conductivity measurements follow the API standard. This procedure uses sandstone samples with a smooth surface and high concentration of proppants. While this procedure is an effective way to examine the quality of the proppants, it is not representative of the fracture conductivity in shale formations for the common low proppant concentration job. Furthermore, the Eagle Ford shale is a heterogeneous formation as seen by the wide range of flow rates and fluids produced in wells located a few miles apart (**Fig. 1.6**). The heterogeneity was captured by a study performed by Donovan et al. (2012) where five different geological facies for the

Eagle Ford shale were defined. There is not much public literature that analyzes the impact that different lithologies within a formation have on fracture conductivity.

The work here focuses on the unpropped, fracture conductivity without proppants, and propped fracture conductivity of the Eagle Ford shale. Realistic proppant concentration and proppant types for this formation are used. The fracture orientation with respect to the bedding planes and the fracture surface attributes are analyzed and their impact on conductivity is discussed. Heterogeneity of the formation is addressed by testing fracture conductivity samples from the aforementioned five different facies present in the Eagle Ford shale. The mineralogy of the samples was determined in order to validate our samples relationship to the Eagle Ford shale and to analyze its impact on fracture conductivity.

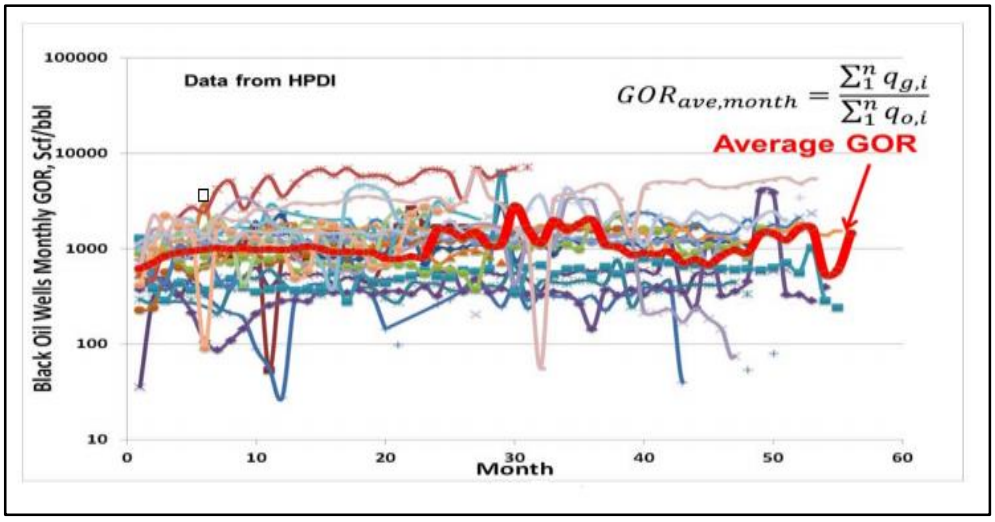

Fig. 1.6 – Gas Oil Ratio for Black Oil Wells in the Eagle Ford Shale (Tian et al. 2013).

The objective of this study is to develop a deep understanding of the Eagle Ford shale unpropped and propped fracture conductivity. This knowledge in turn could be used

to improve the understanding of the production of the Eagle Ford shale and to design the appropriate proppant type and concentration used during the stimulation process. It is worth pointing out that the samples used for this study were gathered at outcrops. With this in mind the deliverables of this project are the following:

(1) To adapt and improve the laboratory procedures to measure fracture conductivity
(2) To measure unpropped and propped fracture conductivity of the five different geological facies of the Eagle Ford shale-outcrop samples.
(3) To investigate the relationship(s) between fracture conductivity and surface attributes, fracture orientation and geological facies.
(4) To analyze the difference between propped and unpropped fracture conductivity in the Eagle Ford shale-outcrop samples.

1.4 Approach

The experimental procedures used in this work can be divided into three main sections. The first section consists of defining the experiments that will be performed. The second section involves performing the laboratory experiments in order to gather data and the last section is analyzing the data. Experiments were designed to measure the unpropped and propped fracture conductivity under realistic conditions for the five different geological facies of the Eagle Ford shale. In order to perform the experiments, samples were collected from the five different zones of the Eagle Ford shale. Three different fracture orientations are considered in this study. After the collection process the rocks are sent to Kocurek Industries where they are cut and fracture under mode I tension into modified API

conductivity dimensions. Fracture conductivity at different closure stresses is determined based on laboratory measurements following the procedure developed from previous studies (Kamenov 2013; Aweloke 2013; Briggs 2014; Guzek 2014; Zhang 2014; McGinley 2015). The fracture area and fracture roughness are calculated from data taken with a surface profile meter. The mineralogy of the samples is determined in order to validate our sample's relationship to the Eagle Ford shale and to analyze the impact this parameter has on fracture conductivity. In addition to these experiments pictures of every sample are taken. Once the data is collected, the unpropped and propped conductivities as well as the proppant effect for each zone are analyzed and discussed. Conductivity dependence on fracture area, fracture roughness and mineralogy is explored. After analyzing each zone, comparisons across zones are made, then conclusions for each zone are presented and general conclusions are drawn by combining the analyses of the five different zones.

1.5 Structure of Thesis

The structure of this thesis is the following. Section 1 includes a literature review of the fracture conductivity, its controlling parameters and the Eagle Ford shale and its importance. In this section the link between these topics is made and importance of studying the fracture conductivity of the Eagle Ford shale is presented.

Section 2 introduces the samples and their relationship to the Eagle Ford shale. The experimental design and procedures are introduced as well as the methods used to calculate the fracture conductivity.

Section 3 focuses on the experimental results. The conductivities for each geological facies are analyzed and their relationship to the surface attributes is explored.

Section 4 builds on the results presented in the previous section and uses them to create comparisons across the five different geological facies. The mechanical properties used in this study are introduced. Based upon this, the controlling parameters on fracture conductivity for the Eagle Ford shale are found.

Section 5 summarizes the results, presents the limitations of this work and provides recommendations for future work.

2. EXPERIMENTAL DESIGN AND METHODOLOGY

This section presents a description of the samples, laboratory design, equipment and laboratory procedures used to calculate fracture conductivity.

2.1 Sample Collection

Eagle Ford shale samples were collected at Antonio Creek and Lozier Canyon. Both outcrops are several hundred feet thick and extend for a few thousand feet laterally. The outcrops are separated by a few miles and as you move from Lozier canyon towards Antonio creek, different facies of the Eagle Ford shale are accessible for collection. These outcrops are located in West Texas (**Fig. 2.1**). At these locations Donovan et al. (2012) defined five different geological facies (A, B, C, D and E) each with distinct lithological characteristics and geochemical response that can be correlated to the subsurface of South Texas. In this classification, facies A lies right above the Buda limestone, followed by facies B which has the highest total organic content and production. Facies A and B are known as the lower Eagle Ford shale, whereas Facies C, D and E are also known as the upper Eagle Ford shale. Facies E underlies the Austin chalk. (**Fig. 2.2**).

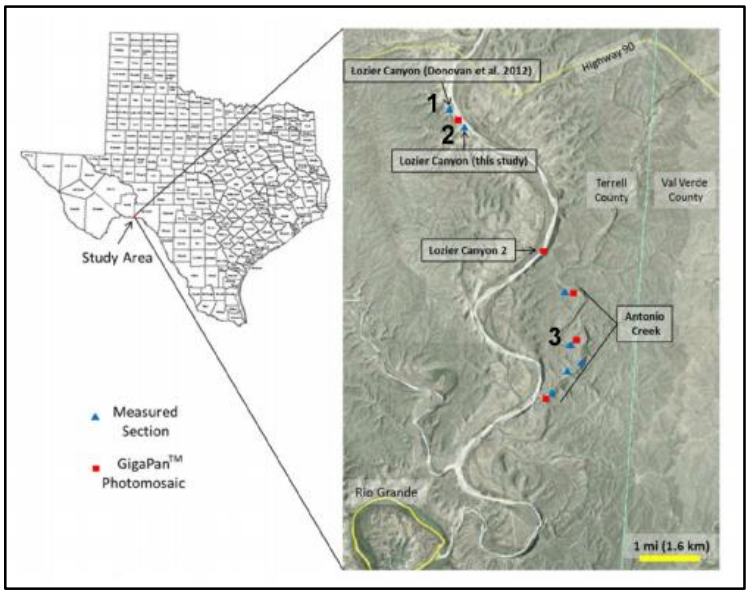

Fig. 2.1 – Map of the Geographic Location of Antonio Creek and Lozier Canyon (Gardner et al. 2013).

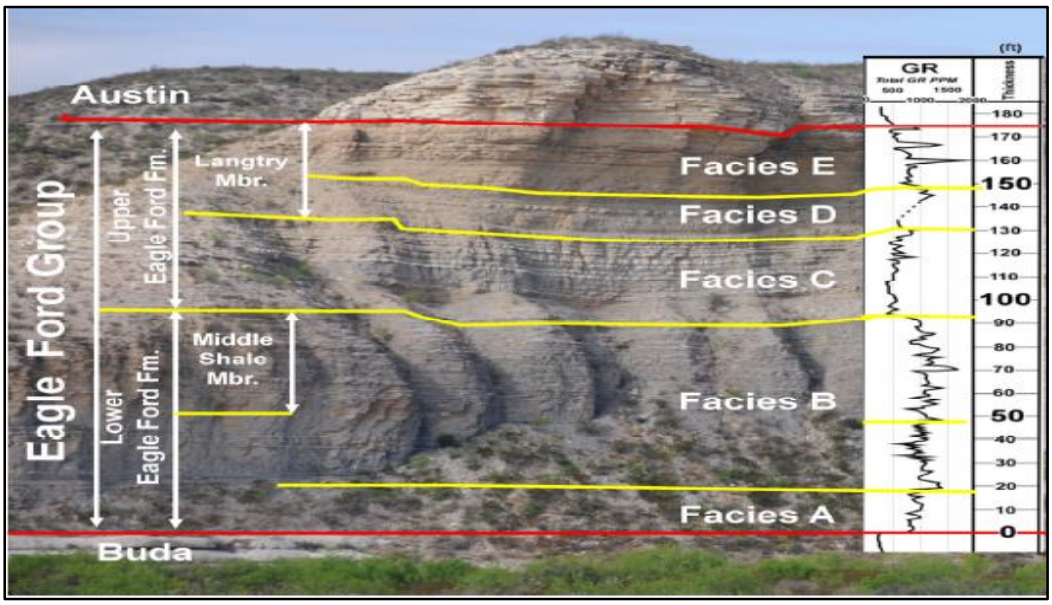

Fig. 2.2 – Five Different Geological Facies of the Eagle Ford Shale with Their Corresponding Gamma Ray Response and the Industry Nomenclature for the Formation- at Lozier Canyon, Southwest Texas (Donovan et al. 2012).

Rock samples were collected from the five different geological facies. Mineralogy of the samples via x-ray diffraction was determined by Knorr (2016). A summary of each facies as described by Donovan et al. (2012) is presented as well as the determined mineralogy in order to link the samples to the outcrops.

Facies A which lies at the bottom of the formation is formed by light gray limestone (grainstones/packstones) separated by thin calcareous mudstone beds. The mineralogy of the collected samples was found to be 84% Calcite, 7% Quartz, 3% Dolomite, 1% Chlorite, 2% Albite and 3% Kaolinite (**Fig. 2.3**).

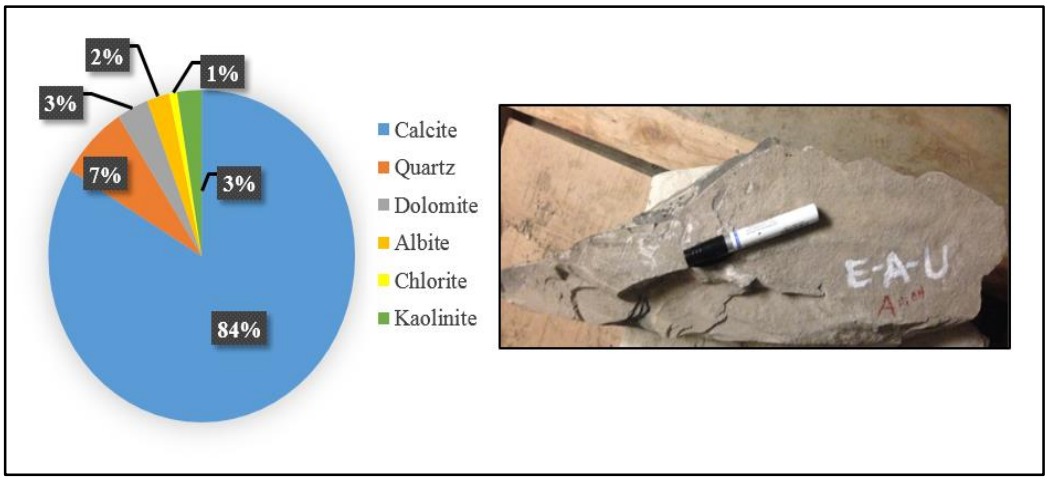

Fig. 2.3 – Mineralogy (Weight Percent) and Collected Rock Sample (Sharpie for Scale) – Facies A.

Facies B is a black organic rich calcareous mudstone with some interbedded limestone. The mineralogy of the collected samples was found to be 70% Calcite, 18% Quartz, 2% Dolomite, 1% Pyrite and 9% Kaolinite (**Fig. 2.4**).

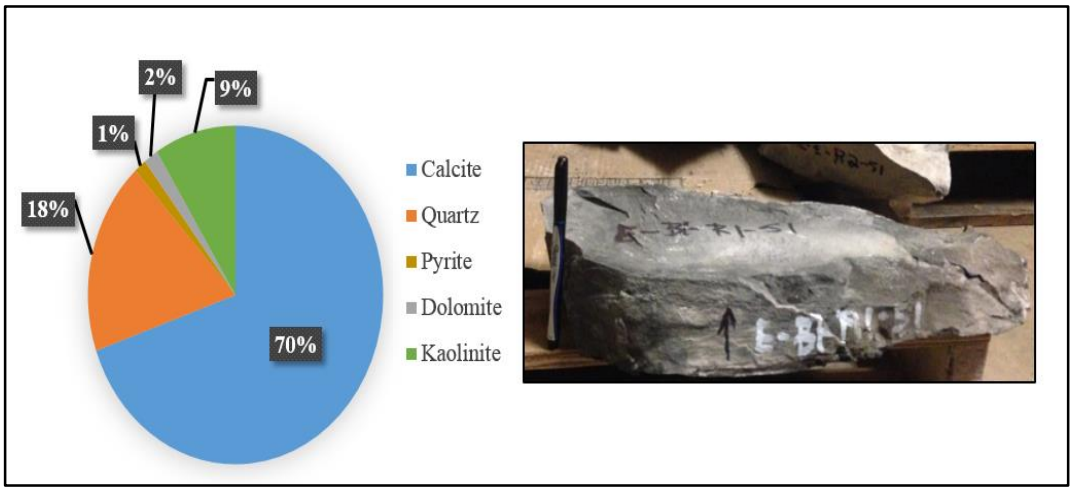

Fig. 2.4 – Mineralogy (Weight Percent) and Collected Rock Sample (Pen for Scale) – Facies B.

Facies C is formed by grainstone prone limestone with mudstone intervals. The mineralogy of the collected samples was found to be 77% Calcite, 11% Quartz, 1% Pyrite, 3% Chlorite, 2% Kaolinite and 5% Illite (**Fig. 2.5**). Facies D is a marl (calcium carbonated with some sand, silt and/or clays) with some limestone. The color of this facies is pale yellow ochre. The mineralogy of the collected samples was found to be 93% Calcite, 2% Quartz, 1% Pyrite, 1% Dolomite and 3% Kaolinite (**Fig. 2.6**).

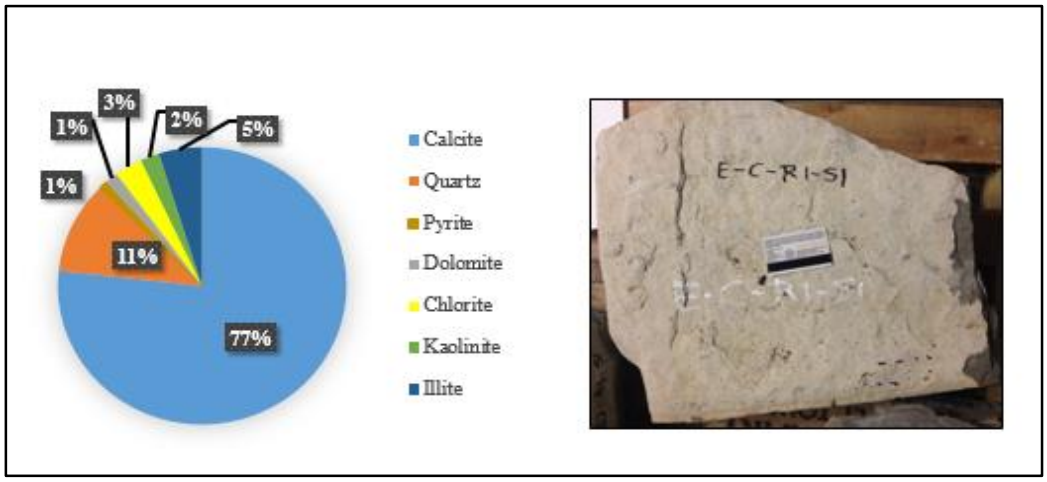

Fig. 2.5 – Mineralogy (Weight Percent) and Collected Rock Sample (Credit Card for Scale) – Facies C.

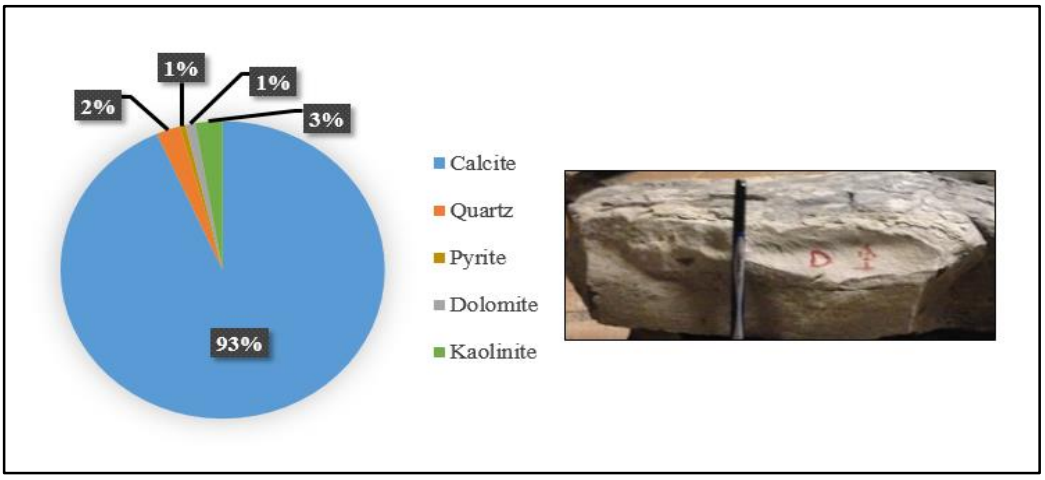

Fig. 2.6 – Mineralogy (Weight Percent) and Collected Rock Sample (Pen for Scale) – Facies D.

Facies E is formed by thin interbedded limestones (grainstone) and calcareous mudstone. The color of this facies is yellow ochre. The mineralogy of the collected samples was found to be 93% Calcite, 2% Quartz, 1% Pyrite, 1% Dolomite and 3% Kaolinite (**Fig. 2.7**).

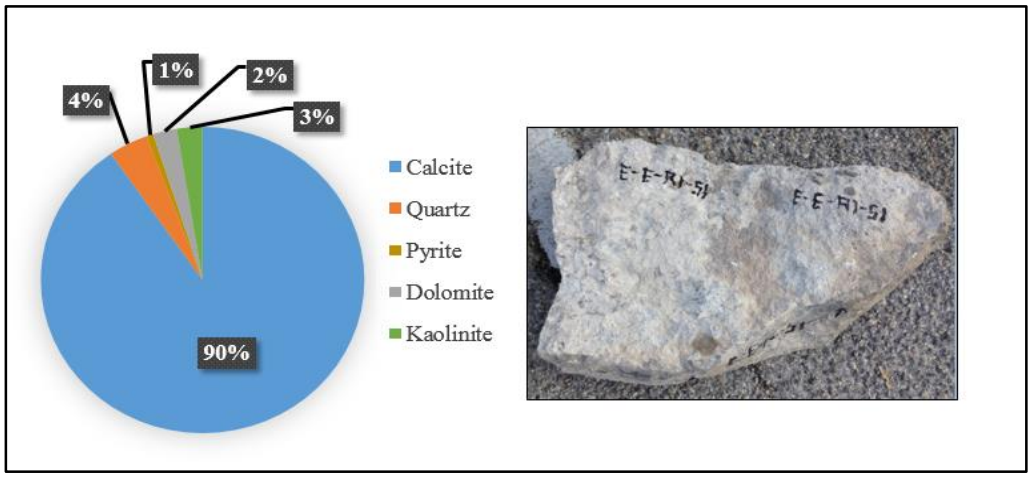

Fig. 2.7 – Mineralogy (Weight Percent) and Collected Rock Sample – Facies E.

The samples collected for this study match the expected mineralogy of the outcrops. The high quartz content in zone B can be explained by the positive relationship between quartz and total organic content. Miceli-Romero (2014) determined the total organic content of samples from Lozier canyon via Rock Eval Pyrolysis (Table. 2.1).

Table. 2.1 – Total Organic Content (Weight Percent) Samples from Lozier Canyon. Sub-Facies B1 and B2 Combined into Facies B.

Facies	TOC, %
A	2.8
B	5.5
C	1.1
D	0.6
E	0.1

In order to link the outcrops to the subsurface, four major sequences divided by beds (K63sb, K64sb, K65sb, K70sb and K72sb) with specific well log responses were identified. (**Fig. 2.8**). The sequences were first identified at the outcrops and then correlated to wells in the Eagle Ford shale (**Fig. 2.9**).

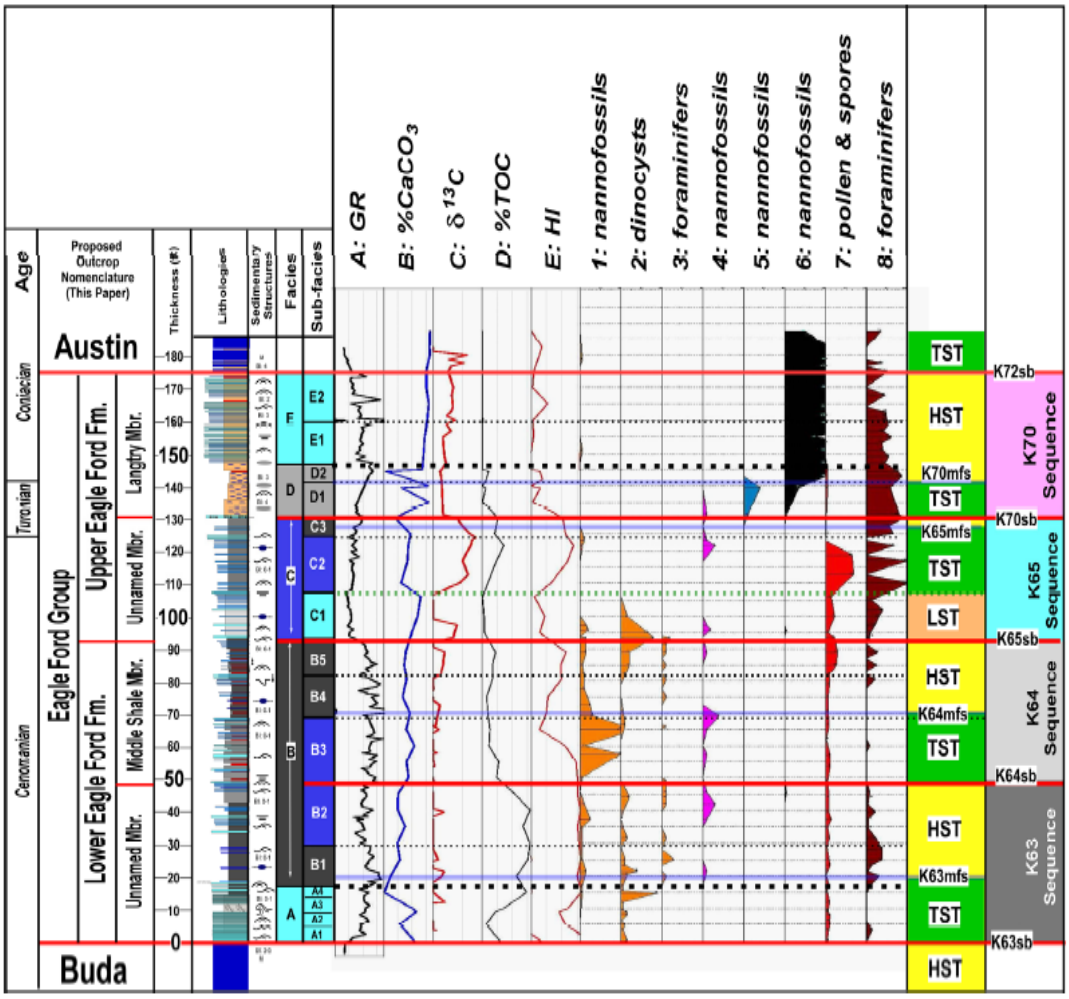

Fig. 2.8 – Biostratigraphic, Geochemical, Petrophysical and Lithofacies Interpretation of Lozier Canyon and Sequence Interpretation (Donovan et al. 2012).

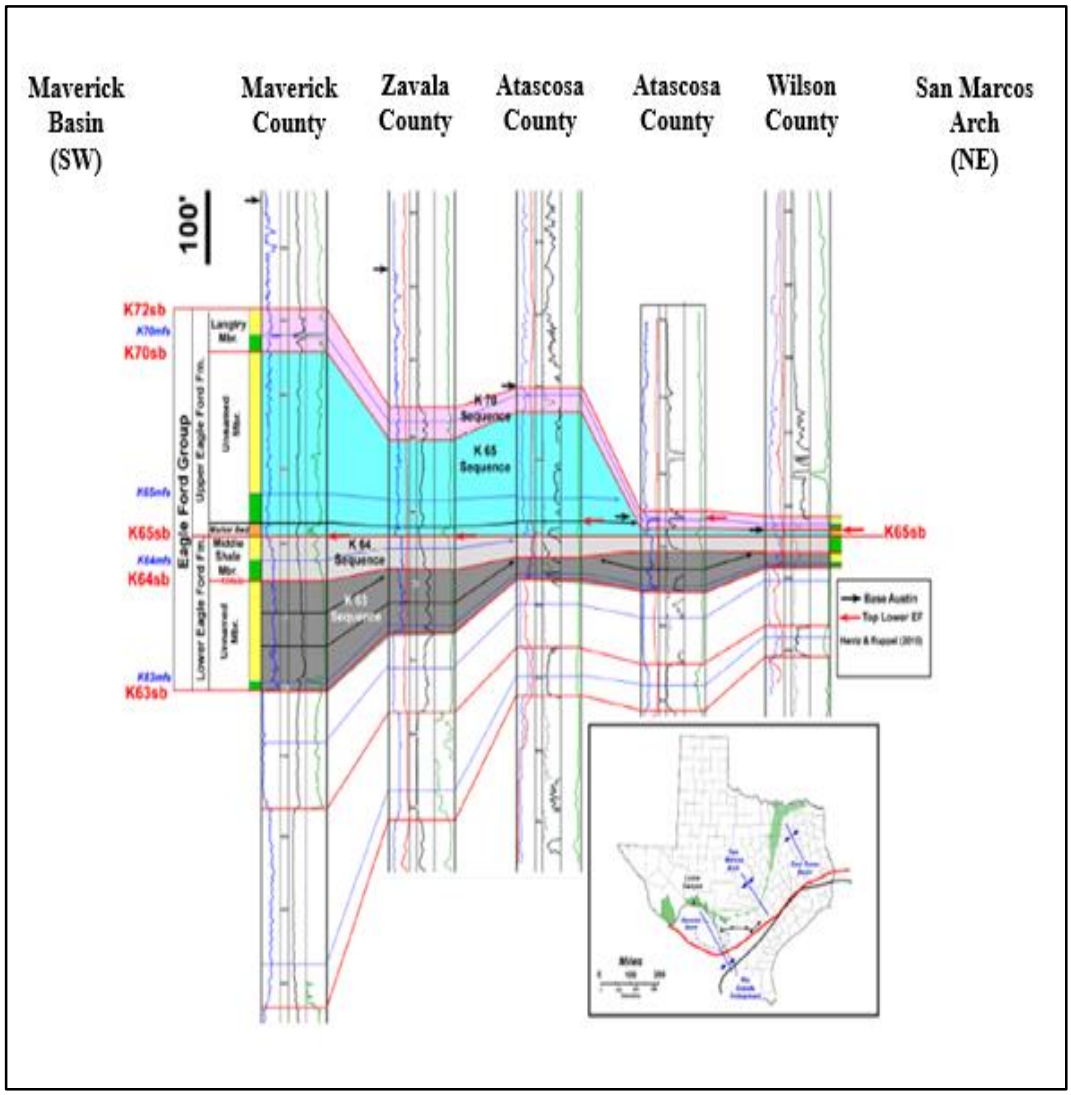

Fig. 2.9 – Well Log Correlation from the Maverick Basin to the San Marcos Arch Modified from Donovan et al. (2012).

The samples collected and used in this study are representative of the outcrops where they were collected. In turn these outcrops are representative and can be traced to the Eagle Ford shale in the subsurface. Therefore, the samples collected and used in this study are a good representation of Eagle Ford shale.

2.2 Sample Preparation for Fracture Conductivity Test

Fractures propagate perpendicular to the minimum principal stress. On a typical sedimentary basin the overburden is the maximum principal stress and the other two principal stresses are located on the horizontal plane. Therefore a fracture will propagate on a plane perpendicular (fracture plane) to the minimum principal horizontal stress. The fracture plane will cut across bedding planes and when a complex fracture network is created, fractures along the bedding are needed to connect the different fracture planes. In order to represent these orientations, samples in three directions with respect to the bedding plane were obtained (**Fig. 2.10**).

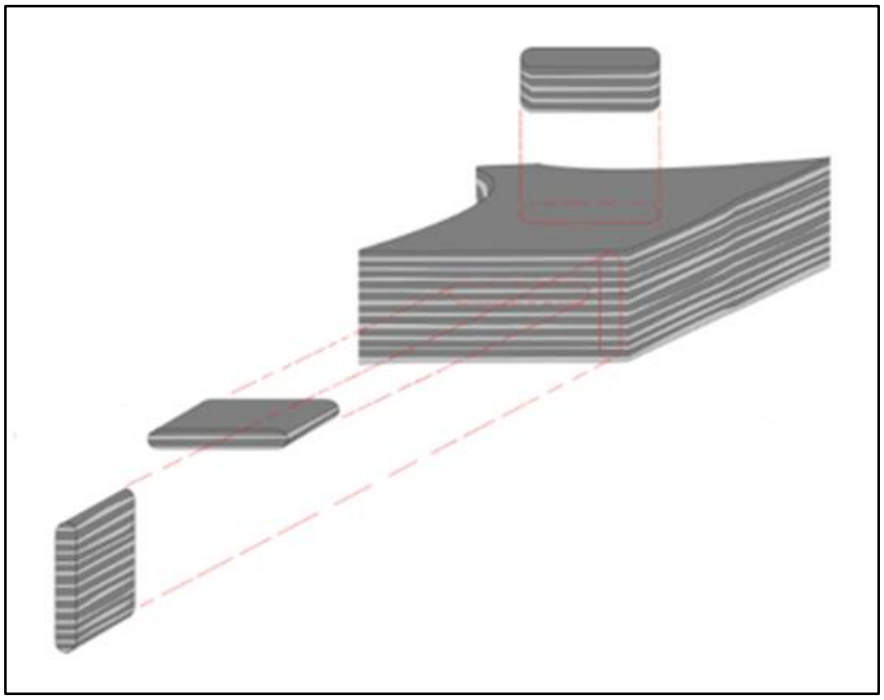

Fig. 2.10 – Orientation of Conductivity Samples Obtained from the Outcrops.

The rock samples were cut and fractured into modified API conductivity cell dimensions (7 inches long, 1.65 inches wide and at least 3 inches thick) by Kocurek industries. Sandstone inserts were used to reach the 6 inches in thickness required for the modified API conductivity cell (**Fig. 2.11**).

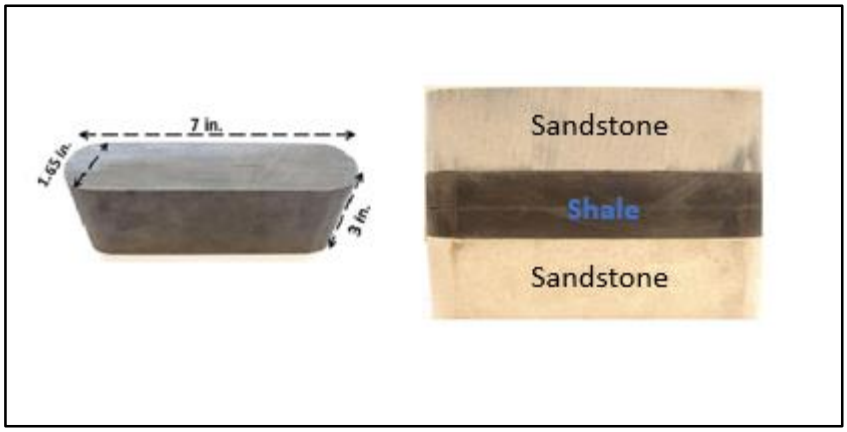

Fig. 2.11 –Modified API Conductivity Sample Dimensions - (Kamenov 2013).

The sample orientations represent three principal flow directions; two in the vertical direction with one parallel to the bedding plane (X0) and another one perpendicular to the bedding plane (X90) as well as one in the horizontal direction (Z). (**Fig. 2.12**). X0 and X90 represent flow in the fracture plane and therefore are more relevant on the Eagle Ford shale. For this reason samples in the X0 and X90 direction were obtained for the five different geological facies. Samples in the Z directions were obtained only for zone B since it is the facies with the highest total organic content and production.

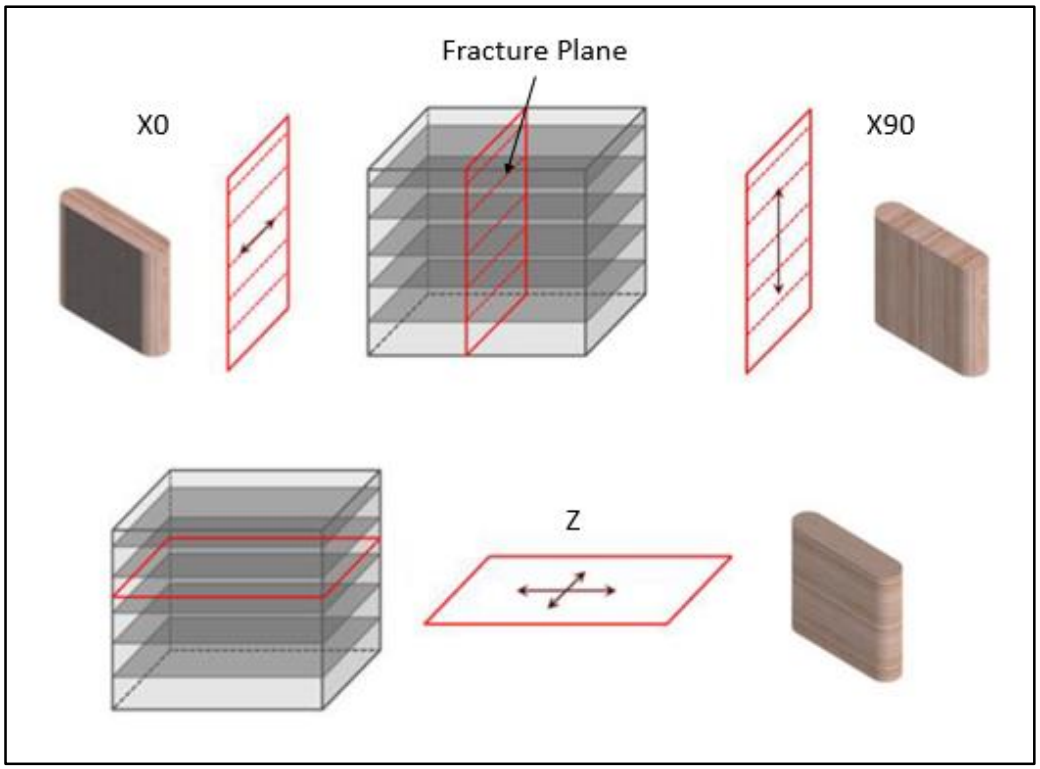

Fig. 2.12 – Sample Orientation: Parallel (X0) and Perpendicular (X90) to the Bedding Plane and on the Bedding plane (Z) Modified from McGinley 2015.

2.3 Proppant Concentration

For this study proppants were placed manually in the fracture face. The proppants used were manufactured in compliance with ISO 13503-2. Proppant concentration is expressed in lbm/gal (Ppg) and also in lbm/ft^2. In this study the conversion of the two units, lbm/gal and lbm/ft^2 was performed by first calculating the fracture area with **Eq. 2-1**. Sample calculation is shown in **Eq. 2-2**.

$$A_{fracture} = A_{rectangle} + 2A_{Halfi-circle} \quad \text{..... (2-1)}$$

$$A_{fracture} = \left((7\ in - 1.65\ in) \times 1.65\ in\right) + \frac{\pi \times 1.65\ in^2}{4}$$

$$= 10.97\ in^2 \frac{ft^2}{144\ in^2} = 0.076\ ft^2 \quad \text{..... (2-2)}$$

Then we calculate the weight of the proppants that will be used for a given surface concentration (in this case 0.1 lbm/ft^2) with **Eq. 2-3**. Sample calculation is shown in **Eq. 2-4**.

$$Proppant\ mass = Desired\ concentration\ \frac{lbm}{ft^2} \times A_{fracture} \text{..... (2-3)}$$

$$Proppant\ mass = \frac{0.1\ lbm}{ft^2} \times 0.076\ ft^2 = 0.0076\ lbm \text{..... (2-4)}$$

To convert a proppant mass per unit area concentration to a proppant mass per unit volume, Ppg, a fracture width needs to be assumed. With this assumption and **Eq. 2-5** the proppant concentration per unit volume is converted from the units of lbm/ft^2. For this sample calculation we assume a fracture width of 0.15 in. Sample calculation is shown in **Eq. 2-6**.

$$Concentration/volume = \frac{Proppant\ mass}{A_{fracture} \times fracture\ width} \text{..... (2-5)}$$

$$\frac{Concentration}{volume} = \frac{0.1\ lbm}{ft^2 \times 0.15\ in \times \frac{ft}{12\ in}} = 8\frac{lbm}{ft^3}\frac{ft^3}{7.48052\ gal}$$

$$= 1.069\ \frac{lbm}{gal} \quad \text{(2-6)}$$

As discussed the equivalent Ppg concentration depends on the fracture width assumed. Table. 2.2 presents the equivalent proppant concentration per unit volume (Ppg) for multiple combinations of assumed fracture widths (in) and proppant concentrations per unit area (lbm/ft^2). As discussed by Zhang (2014) the assumed fracture widths are at the end of the pumping stage and ignores proppant settling before the fractures closed on the proppants.

Table. 2.2 – Equivalent Proppant Concentrations (Ppg) for Multiple Combinations of Fracture Widths (in) and Proppant Concentrations per Unit Area lbm/ft^2.

	Width →	**0.10 in**	**0.15 in**	**0.20 in**	**0.25 in**	
ppg	0.4	0.02	0.04	0.05	0.06	lbm/ft^2
	1.2	0.08	0.11	0.15	0.19	
	1.6	0.1	0.15	0.2	0.25	

As a reference a 100 mesh sand grain in average has a diameter of 0.0059 in. In order to determine the proppant concentration that would be used in this study information from more than three hundred wells from fifty six different companies was analyzed. The data was obtained from drillinginfo (www.drillinginfo.com) and contains wells targeting the Eagle Ford shale in sixteen different counties in Texas (**Fig. 2.13**).

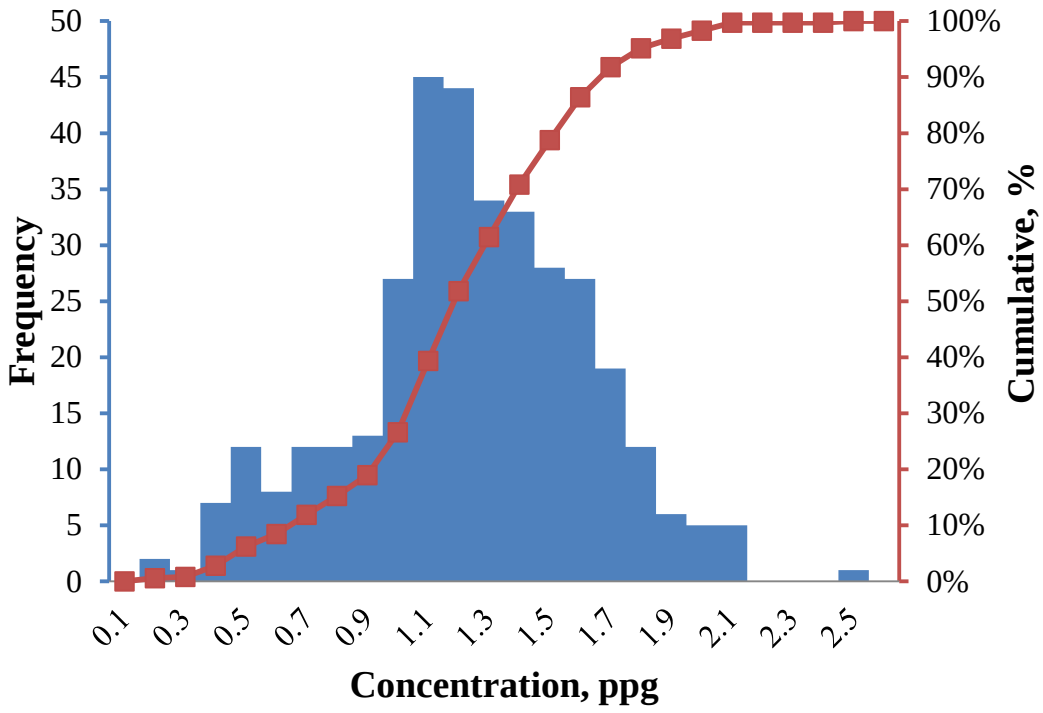

Fig. 2.13– Proppant Concentration (Ppg) Histogram for 353 Wells Located in the Eagle Ford Shale in 16 Different Counties in Texas- Data Obtained from www. Drillinginfo.com.

More than 80% of the analyzed wells contain concentrations between 0.4 Ppg and 1.6 Ppg. The mean, median and mode are also contained in this range. We decided to use a 0.1 (lbm/ft^2) because this concentrations will put the concentration in the 0.4-1.6 Ppg range for multiple fracture width assumptions (Table. 2.2). 100 mesh and 30/50 mesh proppants were chosen as the proppants for the experiments in this study. Both proppants are among the most used in the Eagle Ford shale according to the data analyzed (**Fig. 2.14**). Furthermore, 100 mesh is commonly used during slick-water treatment which are common in natural gas wells. In addition, previous students from our research group

(Zhang 2014; Guzek 2014) used these proppants and concentrations which allows result comparisons.

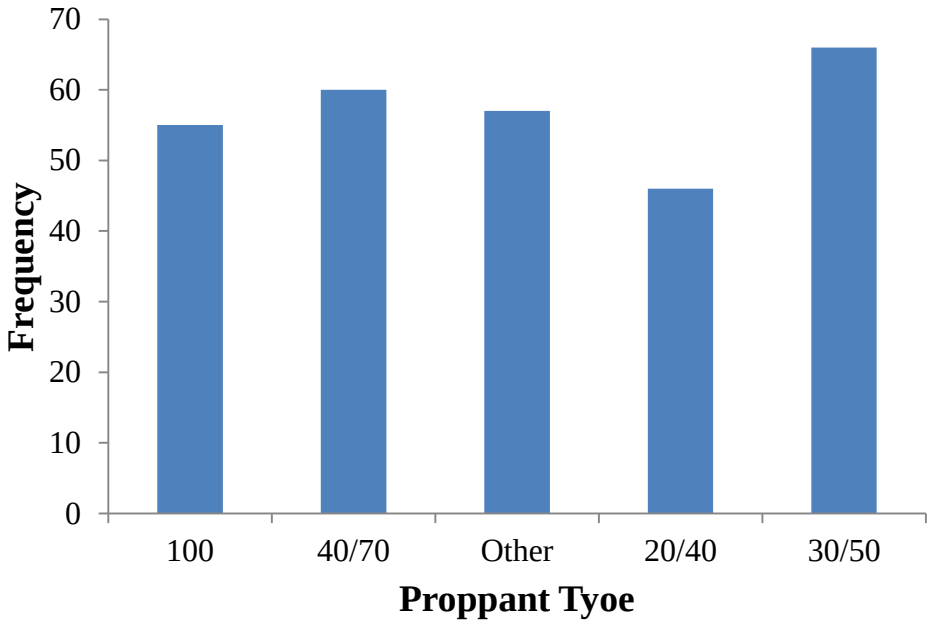

Fig. 2.14– Proppant Type Histogram for 284 Wells Located in the Eagle Ford Shale in 16 Different Counties in Texas- Data Obtained from www. Drillinginfo.com.

The data (www.drillinginfo.com) used to select the proppant type and concentration was not reported in a consistent manner, in order to use this data the following process was used. All the proppant types used in each well were recorded. For the proppant concentration: If the data was reported as an average Ppg using a single proppant for the job it was used as reported. If multiple proppant concentrations and proppants were used and reported a weighted average was calculated and the result was used. If the total proppant mass and total fluid volume were reported, the concentration was calculated by dividing the total mass over the total volume of fluids used. If the data

was reported in a different manner than the ones previously discussed it was not used. We recognize that when the proppants are added into the slurry mix they increase the volume of the mixtures and therefore they change the proppant per unit volume concentrations. However, it was found that this change is insignificant for the concentrations used in this study. This point is illustrated with sample calculations for a 1 Ppg concentration using $2.65 \mathrm{g/cm^3} = 165.43\ \mathrm{lbm/ft^3}$(density of quartz) for proppant grain density. If the proppant volume is ignored **Eq. 2-7** has to be used. Sample calculation is shown in **Eq. 2-8**. Otherwise **Eq. 2-9** is used. Sample calculation is shown in **Eq. 2-10**.

$$Concentraion/volume = \frac{Proppant\ Mass}{V_{fluid}} \quad \text{(2-7)}$$

$$Concentraion\ per\ unit\ volume = \frac{1\ lbm}{1\ gal} \quad \text{(2-8)}$$

$$Concentration\ per\ unit\ volume = \frac{Proppant\ Mass}{V_{Fluid} + V_{proppant}} \quad \text{(2-9)}$$

$$Concentration\ per\ unit\ volume = \frac{1\ lbm}{1\ gal + \frac{1\ lbm}{165.43\ \frac{lbm}{ft^3}\ \frac{ft^3}{7.48\ gal}}}$$

$$= 0.96\ \frac{lbm}{gal} \quad \text{(2-10)}$$

The previous calculations were repeated for different proppant concentrations (ppg) with different assumptions for the proppant grain densities (**Fig. 2.15**).

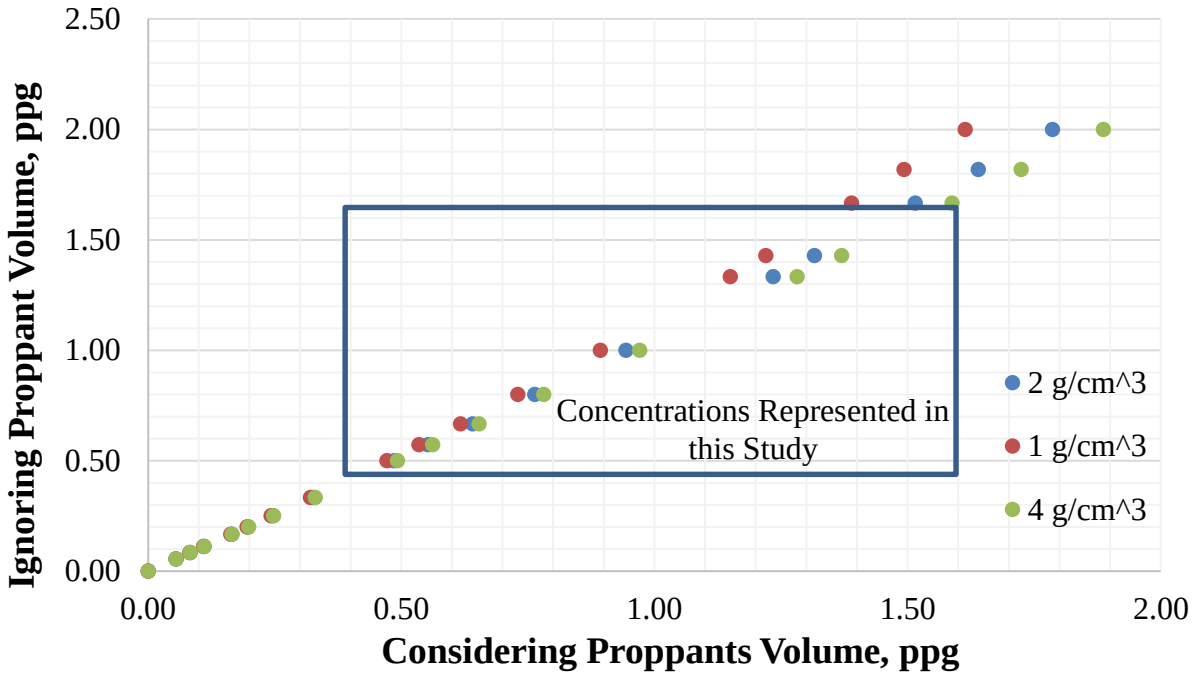

Fig. 2.15 – Proppant Concentration (Ppg) Ignoring and Taking into Account the Proppant Volume for Multiple Proppant (Grain) Densities.

The proppant volume effect on the ppg concentration increases as the concentration per volume increases and as the proppant grain density decreases. From the graph we can see that for normal sands used during slick-water treatments the proppant volume effect on the concentrations is insignificant for the concentrations represented in this study. Therefore, dividing the total mass over the total fluids used in a treatment to calculate the concentration does not introduce a significant error.

2.4 Laboratory Procedures

This section describes the apparatus, experimental design and procedures used for fracture conductivity measurements. The steps followed in this work can be seen in **Fig.2.16**.

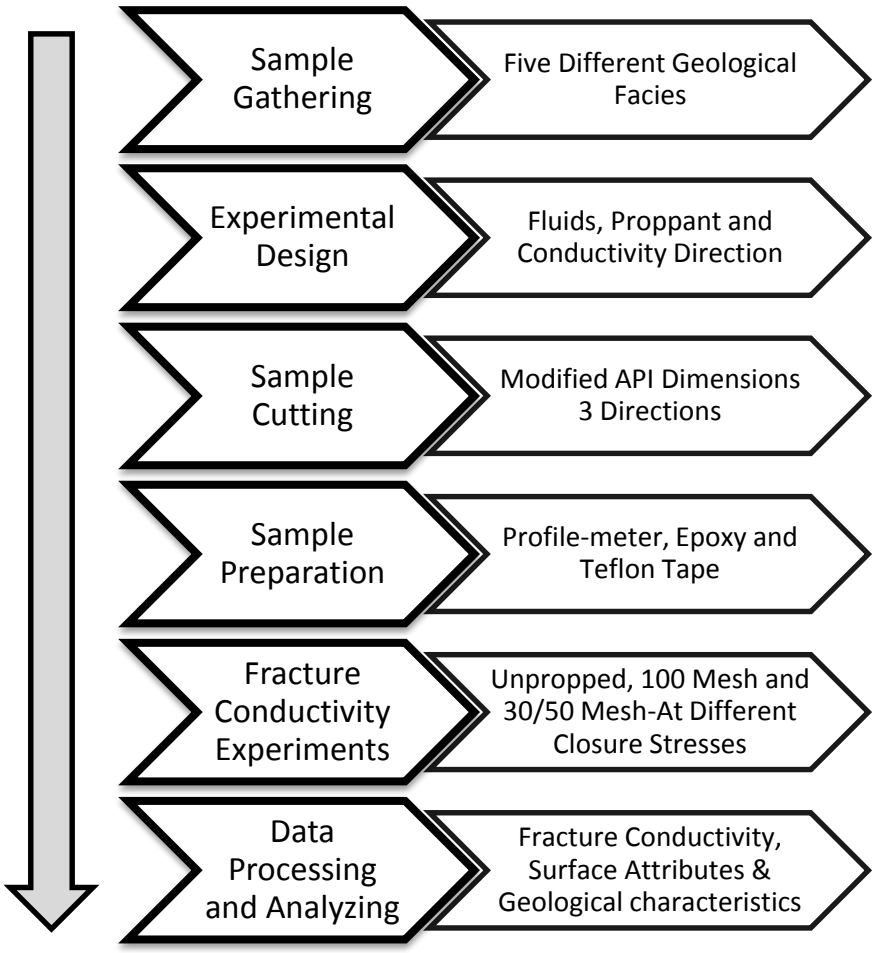

Fig. 2.16 – Process Flow Chart to Calculate and Analyze the Eagle Ford Shale Fracture Conductivity.

2.4.1 Apparatus

Fracture conductivity is determined via laboratory experiments. The main laboratory equipment components used in this study to calculate fracture conductivity and to characterize the surface attributes are the following.

- Hydraulic Load Frame
- Modified API Conductivity Cell

- Mass Flow Meters
- Pressure Transducers
- Surface Profile-Meter

The load frame used is a GCTS FRM4-1000-50S four column vertical standing frame. It has a 1,000 kN static compression load capacity and a 800 kN dynamic load capacity. The stroke length is 5 mm and the maximum velocity is 80 mm per minute. As reported by Kamenov (2013) the modified API cell is made of stainless steel and consists of a cell body, two side pistons and two flow inserts (**Fig. 2.17**). The cell body dimensions are 10 inches long, 3.25 inches wide and 8 inches in height. It can accommodate a core sample 7 inches long, 1.65 inches wide and up to 7 inches thick. Three pressure ports are located in the middle of the cell body. The pistons are 7 inches long, 1.65 inches wide and 3 inches in height and both have a viton polypak seal (O-ring) to prevent leakage. The pistons also have two drilled holes (can be covered) that can be used to simulate fluid leakage if desired. The flow inserts also have viton polypak seal (O-ring) and connect the upstream and downstream flow lines to the cell body.

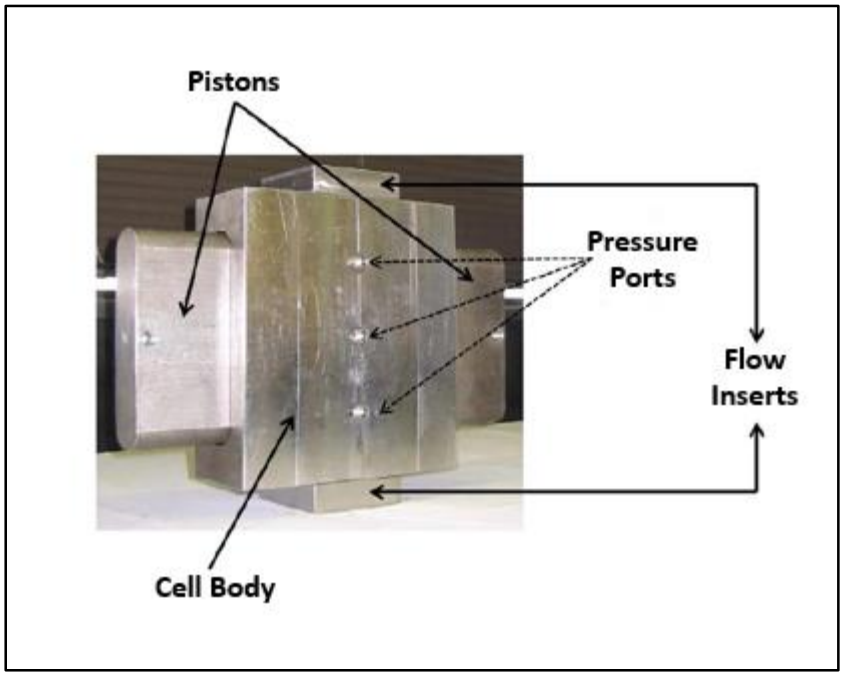

Fig. 2.17 – Modified API Conductivity Cell Modified from Kamenov 2013.

The mass flow meters used were thermal mass flow controllers manufactured by AALBORG. Two flow meters were used. For high flow rates a mass flow meter with range from 0 to 10 standard liters per minute was used. For low flow rates a mass flow meter with range from 0 to 1 standard liters per minute was used. Both flow meters have an accuracy of ± 1% of their maximum flow rate. The maximum working gas pressure is 1,000 psi and the optimum working gas pressure is 20 psi (**Fig. 2.18**). Two pressure transducers were used during the experiments, both were Validyne DP 15 (**Fig. 2.19**). One measures the pressure inside the conductivity cell and the other measures differential pressure along the flow path (fracture). The diaphragms can be easily changed to account for different pressure drops expected during the experiment. The transducers have a ± 2.5% accuracy of their full pressure range. A detailed procedure for the calibration process

can be found in Awoleke's work (Aweloke 2013). Further details on troubleshooting the transducers have been presented by Zhang (2014) and McGinley (2015).

Fig. 2.18 – Low and High Flow Rates Mass Flow Meters.

Fig. 2.19 – Pressure Transducers Validyne DP 15 (Validyne Engineering 2016).

A schematic of fracture conductivity experimental setup can be seen in **Fig. 2.20**. The fracture faces were scanned with a surface profilometer and the data obtained was used to calculate the fracture area and roughness (**Fig. 2.21**).

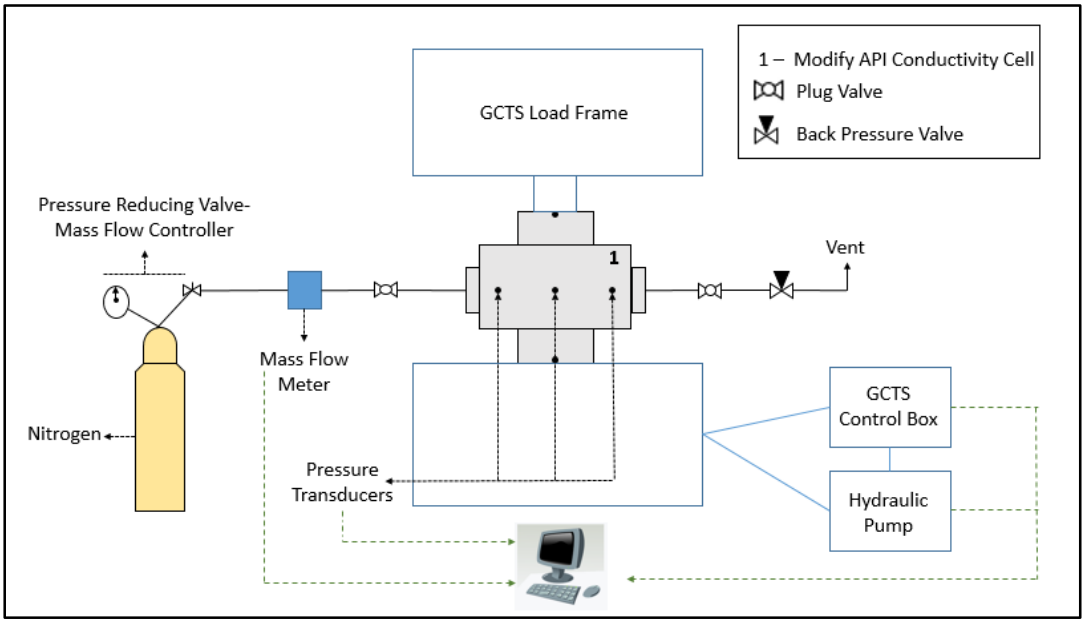

Fig. 2.20 – Schematic of Fracture Conductivity Experimental Setup.

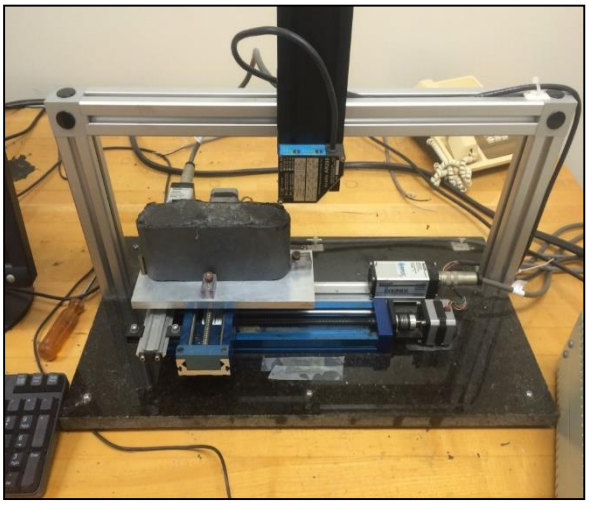

Fig. 2.21 – Surface Profilometer.

2.4.2 Experimental Design

The number of experiments performed was limited by the amount of rock samples collected and/or their dimensions. We obtained as many conductivity samples as possible from the gathered rock samples. The plan was to first measure the unpropped fracture conductivity follow by the conductivity for a 100 mesh proppant concentration of 0.1 lbm/ft^2, and to finish by measuring the conductivity using 30/50 proppant with a concentration of 0.1 lbm/ft^2. This way three tests can be conducted on one sample. Table. 2.3 list the original designed experimental conditions for this study.

Table. 2.3 – Conductivity Samples Obtained from the Collected Eagle Ford Shale Outcrop Rocks.

Geological Facies	Orientation	Number of Samples	Unpropped	0.1 lbm/ft^2-100 Mesh	0.1 lbm/ft^2-30/50 Mesh	Number of Experiments
E	X0	2	2	2	2	6
	X90	2	2	2	2	6
D	X0	2	2	2	2	6
	X90	2	2	2	2	6
C	X0	2	2	2	2	6
	X90	3	3	3	3	9
B	X0	3	3	3	3	9
	X90	4	4	4	4	12
	Z	3	3	3	3	9
A	X0	2	2	2	2	6
	X90	2	2	2	2	6
Total -->		27	26	26	26	81

Some samples were damaged and could not be reuse after the first conductivity experiment. There are also samples that supported two conductivity experiments but could not be used for a third one (**Fig. 2.22**). A small number of samples were able to sustain the three conductivity experiments.

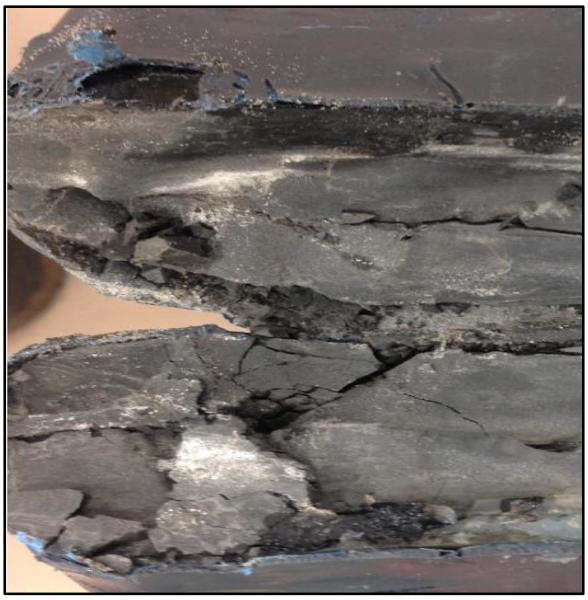

Fig. 2.22 – Damaged Sample from Facies B After 100 Mesh Experiment.

In addition to sample destruction, another limitation was that some unpropped test required a high differential pressure between the cell and the ambient in order to obtain flows within the range of the used mass flow meters. In some cases the differential pressure required was greater than the range of the pressure transducer calibration tool used (30 psi). In these cases unpropped conductivities could not be measured. Taking into consideration these limitations, a summary of the actually performed experiments is presented in **Table. 2.4**.

Table. 2.4 – Performed Fracture Conductivity Experiments for the Eagle Ford Shale Samples

Geological Facies	Orientation	Number of Samples	Unpropped	0.1 lbm/ft^2-100 Mesh	0.1 lbm/ft^2-30/50 Mesh	Number of Experiments
E	X0	2	2	2	1	5
	X90	2	1	2	2	5
D	X0	2	2	2	1	5
	X90	2	1	2	1	4
C	X0	2	1	2	0	3
	X90	3	2	3	2	7
B	X0	3	2	3	1	6
	X90	4	2	4	3	9
	Z	3	3	3	1	7
A	X0	2	2	1	0	3
	X90	2	2	2	1	5
Total -->		27	20	26	13	59

2.4.3 Methodology of Surface Roughness and Surface Area Measurements

The first step taken after receiving the conductivity samples from Kocurek industries was to label them for future references. Samples names have the following format: first letter of formation name for example E for Eagle Ford followed by the geological facies (A-E), followed by an underscore and the sample orientation (X0, X90 and Z), followed by another underscore and the sample number. The experimental files have the experiment type added to the sample name at the end after an underscore (U for unpropped, 100 for 0.1 lbm/ft^2 100 mesh and 30/50 for 0.1 lbm/ft^2 30/50 mesh). For example sample

EB_X0_1_U is a sample from the Eagle Ford shale that represents flow in the X0 direction, parallel to the bedding plane, which is the first sample with these conditions and the experiment was run with no proppants. Next, pictures of the samples were taken. After these steps are completed the samples are ready to be scan.

The samples are placed on the profilometer (**Fig. 2.21**) where both fracture surfaces are scanned. The apparatus has a full scale resolution of 1 inch and an accuracy of ±0.000001 inches. The scanned dimensions are 7 inches long, 1.7 inches wide and the data is collected every 0.05 inches. The profilometer generates a text file with three columns: x position, y position and z reading. This file is the input to a MATLAB code where the fracture roughness and area are calculated. The code only uses data points collected in a rectangular area in the middle of the sample. This is to remove the edges of the sample where the profilometer readings are not reliable. For comparison the area of the rectangle where data is used is 8.81 in^2 and the area of the conductivity cell is 10.97 in^2. Surface roughness was calculated with **Eq. 2-11** and **Eq. 2-12** via the root mean square method (R_{RMS}).

$$R_{RMS} = \sqrt{\frac{1}{n}\sum_{i=1}^{n} z_i^2} \quad \text{(2-11)}$$

$$z_i = |z - \bar{z}| \quad \text{(2-12)}$$

Where $\bar{z}$ is the average reading of all the points measured by the profilometer (inside the rectangle) and z is the profile-meter reading at a specific point. The fracture area was calculated by dividing the rectangular area into parallelograms and using the cross product to calculate the area of each parallelogram with **Eq. 2-13**.

$$Area\ of\ Parallelogram\ Formed\ by\ \vec{x}\ and\ \vec{y} = |\vec{x} \times \vec{y}| \text{..... (2-13)}$$

The area of all the parallelograms were added in order to calculate the rectangular area (fracture area). The process to generate the text file from the profilometer file was presented by (McGinley 2015). The output of the MATLAB code is shown in **Fig. 2.23**. Fracture area and roughness were calculated for all samples.

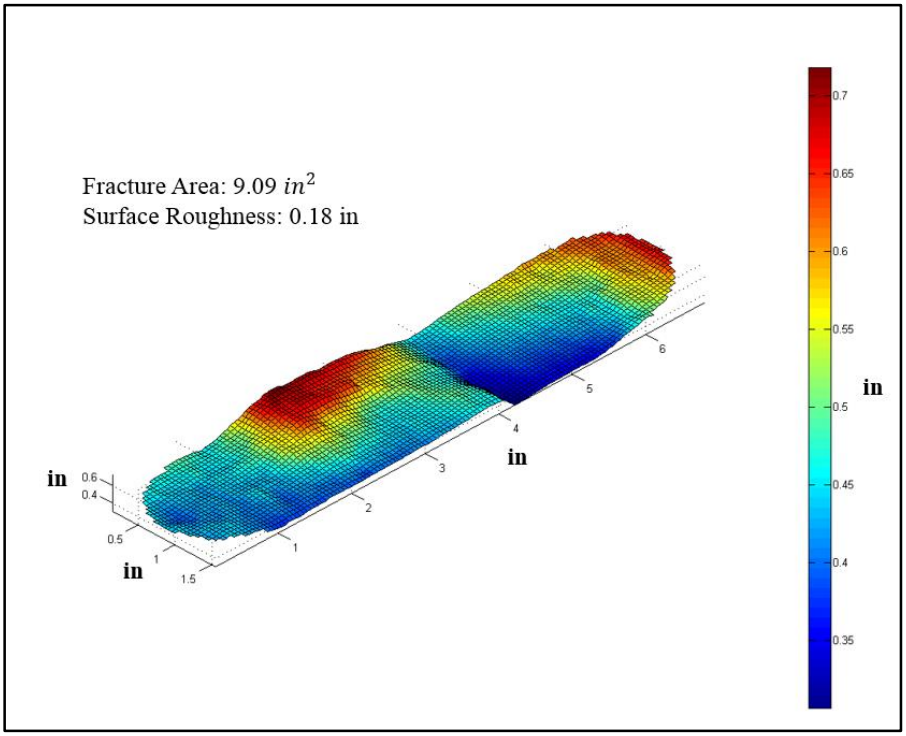

Fig. 2.23 – Fracture Area and Roughness from Profilometer Measurements.

2.4.4 Methodology of Sample Preparation

In order to create a good seal between the conductivity sample and the modified API conductivity cell an epoxy (Momentive RTV 627) was applied to the conductivity samples. The epoxy was applied in a mold 0.1 inches wider than the conductivity sample and 0.003 inches wider than the modified API conductivity sample (**Fig. 2.24**). This creates a tight fit between the conductivity sample and the modified API conductivity which makes significant leakages unlikely even at high pressures. The procedure to apply the epoxy and the common mistakes during the process have been covered by previous studies. (Kamenov 2013; Briggs 2014; Guzek 2014; Zhang 2014; McGinley 2015).

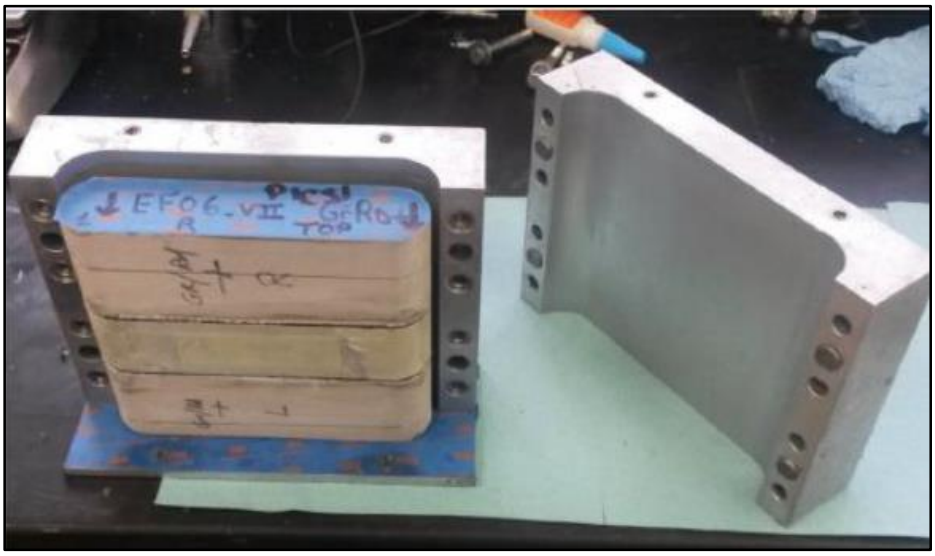

Fig. 2.24 – Aligned Conductivity Sample in the Sample Preparation Mold (Guzek 2014).

The only part of the sample preparation procedures that have not been discussed before is how to remove the conductivity cell from the sample preparation mold. This

procedure starts after the sample have been taken out of the oven for a few hours and the mold is at room temperature.

(1) Remove the mold baseplate and all the screws (4) of the sample preparation mold

(2) Place the sample preparation mold under a hydraulic press

Note: there should be no obstruction at the location of the conductivity sample

(3) Gently apply force with the hydraulic press to the conductivity sample, this should open the preparation mold and release the sample

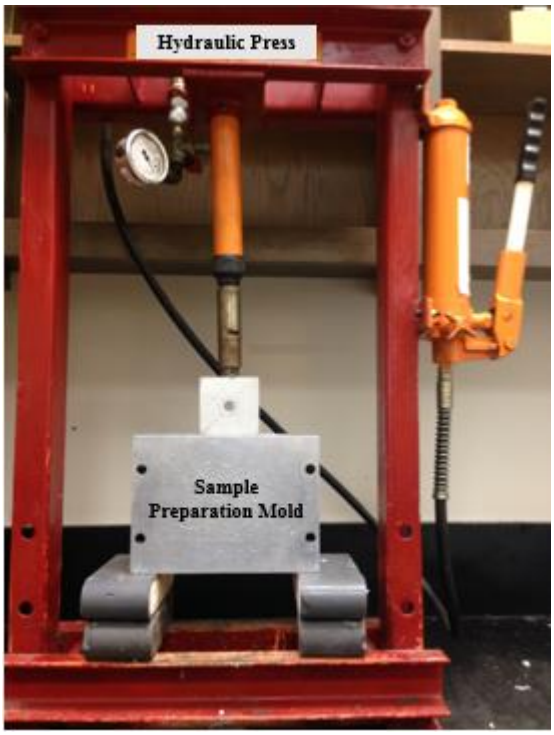

Fig. 2.25 – Removing the Conductivity Sample Coated With Epoxy from the Sample Preparation Mold.

(4) Cut the epoxy to expose the flow inlet and outlet flow ports as well as the three pressure ports. A detailed procedure for this was presented by McGinley (2015)

(5) Use a high density gas line Teflon tape to isolate the pressure ports and minimize leakage. Apply two lines of Teflon tape below the pressure ports, two lines above the pressure ports and two lines in between the pressure ports.

Note: Each Teflon tape line is formed by three wraps of the tape around the conductivity sample

(6) Apply vacuum grease in the spaces between the Teflon tape lines

Note: Do not apply vacuum grease near the pressure ports

(7) The Sample is ready to be placed in the Modified API conductivity sample for unpropped experiments. Briggs (2014) described this process.

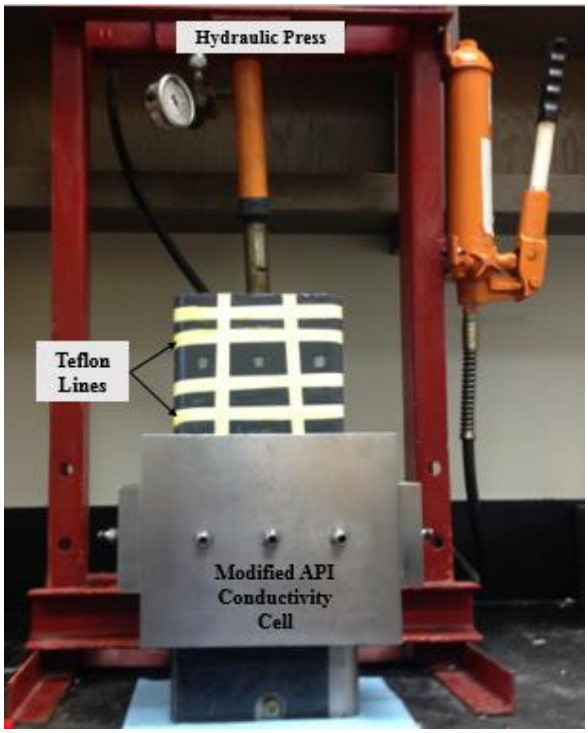

Fig. 2.26 – Conductivity Sample Ready to be Inserted into the Modify API Conductivity Cell for Measurements.

For propped conductivity experiments an extra step involving the proppant placement has to be taken.

(1) Using the digital scale, measure the desired proppant mass for the experiment

(2) Cut a line in the epoxy connecting the pressure ports and the flow inlet and outlet in the front side of the sample

Note: Do not cut the epoxy on the back of the sample, doing so increases the possibility of race tracking

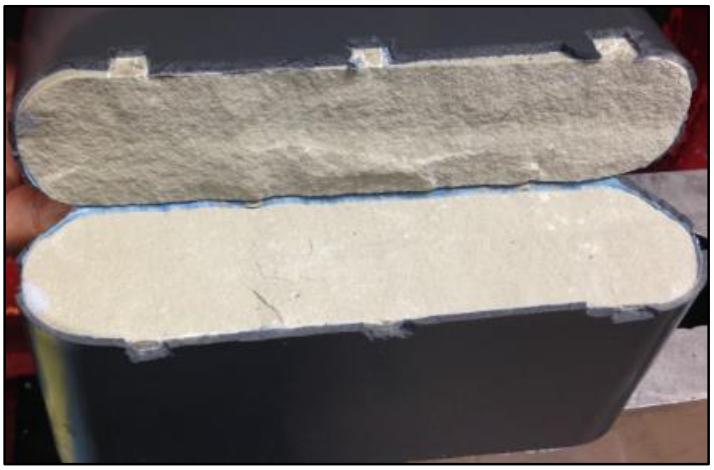

Fig. 2.27 – Cutting the Epoxy from the Conductivity Sample for Proppant Placement.

(3) Gently pull the conductivity sample apart and place the proppant evenly on the surface

Note: This is a two person operation, one places the proppant while the other hold the sample.

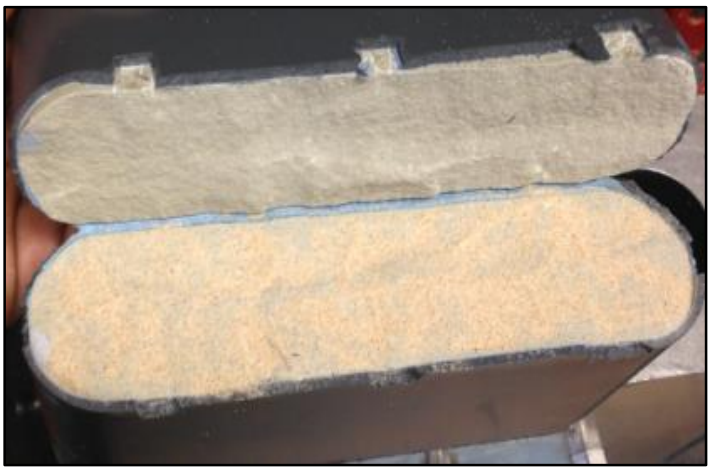

Fig. 2.28 – Conductivity Sample with 0.1 lbm/ft^2- 100 Mesh.

After the proppant is place in the fracture area, Teflon tape is wrapped around the sample. Now the sample is placed in the API modified conductivity cell for fracture conductivity measurements.

2.4.5 Methodology of Gas Fracture Conductivity Determination

Industrial grade nitrogen was used to measure fracture conductivity. Using nitrogen allows us to simulate natural gas flow and does not damage the samples which allows us to re-use them in multiple experiments. Once the sample is placed in the modified API conductivity cell (**Fig. 2.26**) the flow inserts, top piston, pressure transducers and the flow inlet and outlet are placed and connected to the modified API conductivity cell. The fully assembled cell is placed under the hydraulic load GCTS FRM4-1000-50S**.** It is critical that the piston from the hydraulic load is centered with respect to the fully assembled cell.

The screws that are located at the top and bottom pistons should only be tightened after the cell has been exposed to at least 500 psi of closure stress (**Fig. 2.29**).

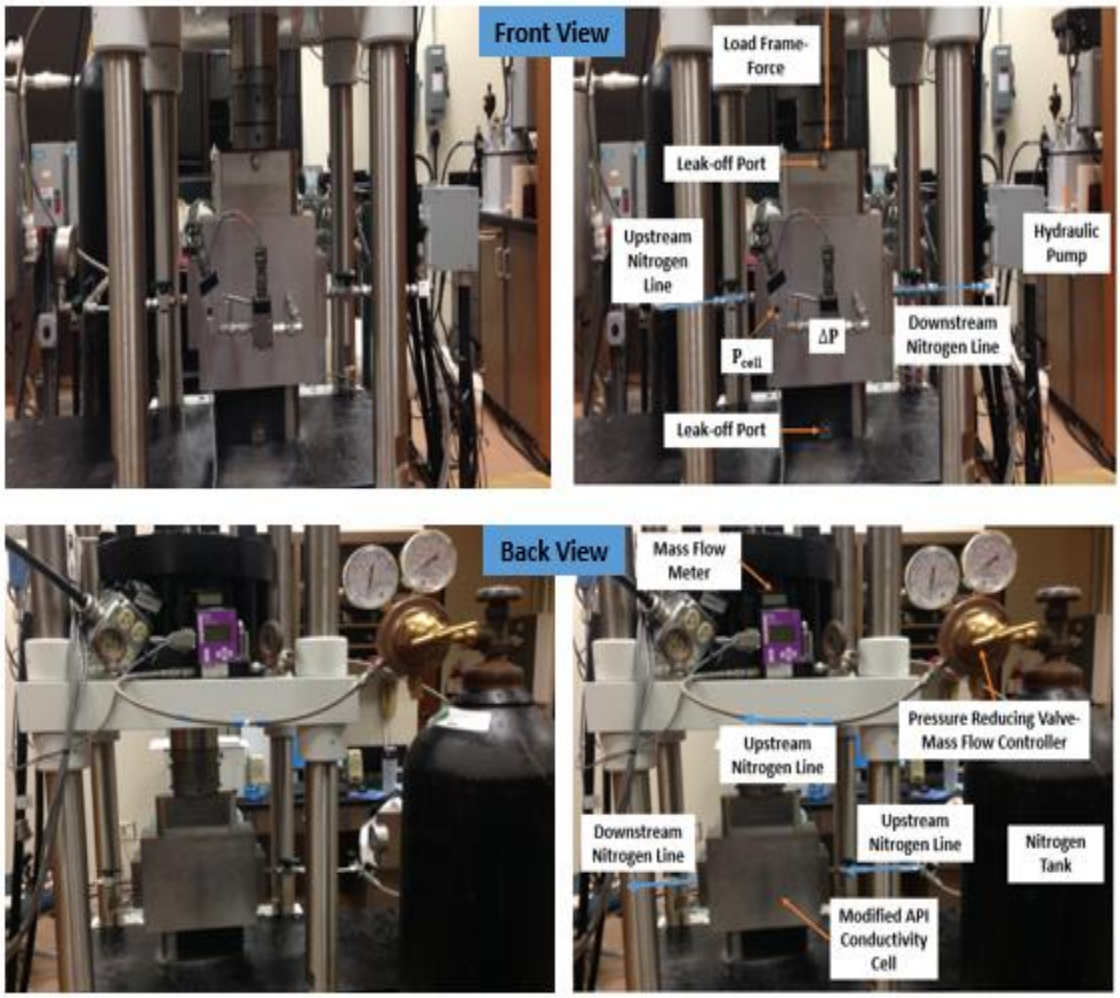

Fig. 2.29 – Fully Assemble Fracture Modified API Conductivity Cell Front and Back Views.

In order to calculate fracture conductivity, nitrogen is flowed through the fracture and the pressure drop created by the flow is recorded. At each closure stress, four flow rates and their corresponding pressure drops are recorded. The Darcy Equation shown in

Eq. 2-14 and the Forchheimer equation shown in **Eq. 2-15** were used to calculate fracture conductivity,

$$-\frac{dp}{dL} = \frac{\mu v}{k_f} \quad \text{(2-14)}$$

$$-\frac{dp}{dL} = \frac{\mu v}{k_f} + \beta \rho_f v^2 \quad \text{(2-15)}$$

Where $-\frac{dp}{dL}$ is the pressure drop per unit length, μ is the fluid viscosity, v is the flow velocity, k_f is the fracture permeability, ρ_f is the fluid density and β is the inertial factor. Zhang (2014) reported that for a concentration of 0.1 lbm/ft^2 and flow rates below 0.8 L/min the Darcy equation is appropriate. For flow rates above 0.8 L/min, the Forchheimer equation should be used. McGinley (2015) reported that for concentrations up to 0.1 lbm/ft^2 and flow rates below 2 L/min, the Darcy equation provided a good fit. For flow rates above 2 L/min, the Forchheimer equation provided a better fit. For this work the Darcy equation is used for flow rates below 1 L/min. For flow rates greater than 1 L/min the Forchheimer equation is used.

In the current laboratory setup the following measurements are made: nitrogen flow rate (q), the cell pressure (P_{cell}) and the pressure drop along the flow path (ΔP). The process used to calculate conductivity via Darcy's Equation explicitly with these laboratory measurements combines the ideal gas law, Darcy's law and conservation of mass. **Eq. 2-14** is multiplied by the fluid density (ρ_f) to obtain **Eq. 2-16**:

$$-\frac{dp}{dL}\rho_f = \frac{\mu v}{k_f}\rho_f \quad \text{(2-16)}$$

The relationship between fluid velocity, fluid density and mass flow rate can be expressed as shown in **Eq. 2-17**,

$$\frac{W}{A} = v\rho_f \quad \text{(2-17)}$$

By the ideal gas law (**Eq. 2-18**):

$$\rho_f = \frac{pM_g}{ZRT} \quad \text{(2-18)}$$

Where p is the pressure, M_g is gas molecular weight, Z is the gas compressibility factor, R is the universal gas constant and T is the temperature. Incorporating **Eq. 2-17** and **Eq. 2-18** into **Eq. 2-16** and rearranging we obtain **Eq. 2-19**,

$$-\frac{pM_g}{ZRT}dp = \frac{\mu W}{k_f A}dL \quad \text{(2-19)}$$

Integrating and rearranging **Eq. 2-19** we obtain **Eq. 2-20**:

$$\frac{(P_1^2-P_2^2)}{2}\frac{M_g}{ZRT}=\frac{\mu W}{k_f A}L \quad \text{(2-20)}$$

The fracture cross sectional area can be express by **Eq. 2-21**,

$$A = w_f h_f \quad \text{(2-21)}$$

The mass flow rate can be express with **Eq. 2-22**,

$$W = q\rho_f \quad \text{(2-22)}$$

Incorporating **Eq. 2-21** and **Eq. 2-22** into **Eq. 2-20** and rearranging yields **Eq. 2-23**:

$$\frac{(P_1^2-P_2^2)}{2L}\frac{M_g}{ZRT}=\frac{\mu q\rho_f}{h_f}\frac{1}{w_f k_f} \quad \text{(2-23)}$$

Where P_1 is the upstream pressure, P_2 is the downstream pressure, L is the length of the flow path, q is the gas flow rate, w_f is the fracture width and h_f is our sample width. Assuming that the differential pressure between the first half of the flow path and the second half are equal, P_1 and P_2 can be expresses with **Eq. 2-24** and **Eq. 2-25** respectively.

$$P_1 = P_{cell} - 0.5\Delta P \quad \text{(2-24)}$$

$$P_2 = P_{cell} + 0.5\Delta P \quad \text{(2-25)}$$

Incorporating the definition of fracture conductivity $Cf = k_f w_f$ and combining **Eq. 2-24** and **Eq. 2-25** with **Eq. 2-23** yields **Eq. 2-26**:

$$\frac{\left[(P_{cell}-0.5\Delta P)^2-(P_{cell}+0.5\Delta P)^2\right]}{2L}\frac{M_g}{ZRT} = \frac{\mu q \rho_f}{h_f}\frac{1}{C_f} \quad \text{(2-26)}$$

The three unknowns from **Eq. 2-26** are the variables measured in the laboratory: nitrogen flow rate (q), cell pressure (P_{cell}) and pressure drop along the flow path (ΔP). M_g, Z, ρ_f and μ are known properties of nitrogen. The pressure drop was kept less than $0.1P_{cell}$ in order to assure that the nitrogen properties do not significantly change during the flow path. The experiments were run at constant room temperature (T). R is the universal gas constant. L and h_f are known sample dimensions.

For Darcy flow, $\frac{\left[(P_{cell}-0.5\Delta P)^2-(P_{cell}+0.5\Delta P)^2\right]}{2L}\frac{M_g}{ZRT}$ versus $\frac{\mu q \rho_f}{h_f}$ are plotted for the four recorded data points at each closure stress. The inverse of the best fit line for this plot is the fracture conductivity. This process is illustrated in **Fig. 2.30**.

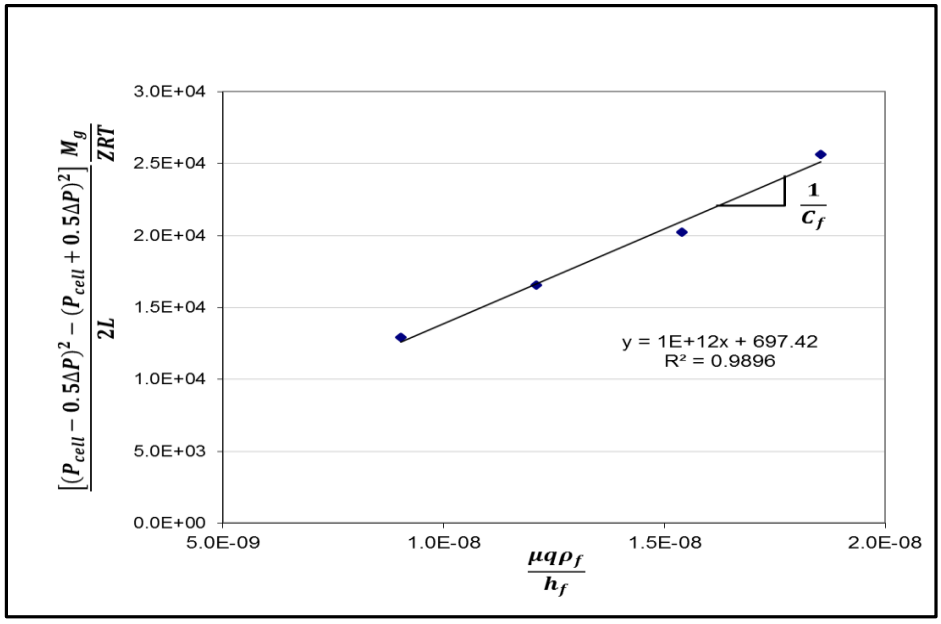

Fig. 2.30 – Fracture Conductivity via Darcy's Law for Sample EE_X90_2_100 at 1000 Psi Closure Stress.

The process is repeated every 1000 psi (starting at 1000 psi) until reaching 6000 psi of closure stress for propped experiments. For unpropped experiments the first reading is at 500 psi, the second at 1000; psi and from this point forward an increment of 1000 psi are made until a closure stress of 4000 psi is reached. The complete results for a fracture conductivity experiment can be seen in **Fig. 2.31**. Fracture conductivity calculation via the Forchheimer equation as presented by Zhang (2014) is calculated by plotting $\frac{P_{cell}M_g\Delta P h_f}{ZRTL\mu q\rho_f}$ versus $\frac{q\rho_f}{h_f\mu}$. In this case the inverse of the y-axis intercept of the best fit line is the fracture conductivity. All the troubles related to the execution of the fracture conductivity experiments encountered in this work have been addressed by previous students of this

research group. (Awoleke 2013; Kamenov 2013; Briggs 2014; Guzek 2014; Zhang 2014; McGinley 2015).

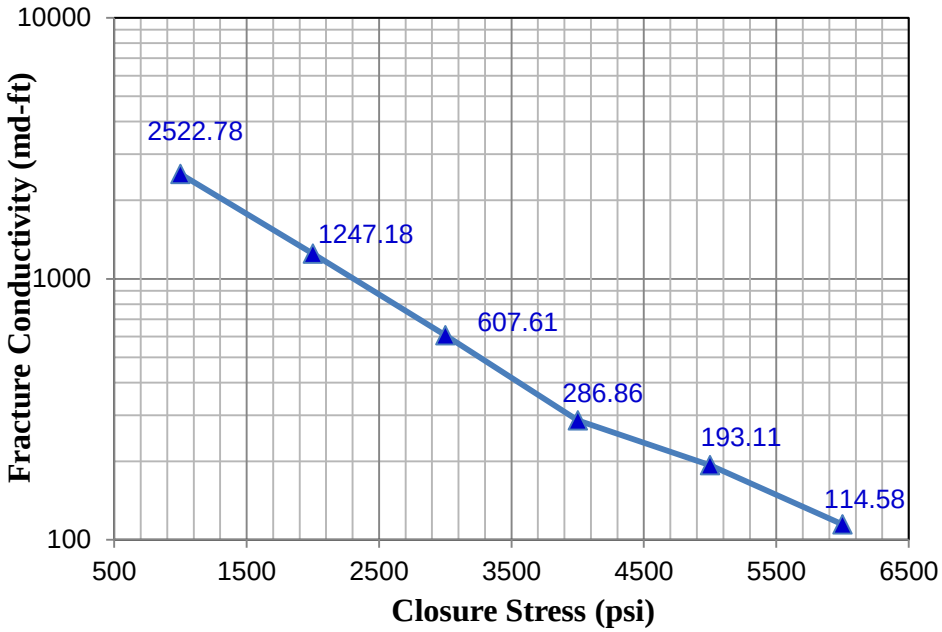

Fig. 2.31 – Fracture Conductivity via Darcy's Law for Sample EE_X90_2_100.

3. FRACTURE CONDUCTIVITY ON FACIES A-E

This section presents and analyzes the fracture conductivity results for each of the five geological facies of the Eagle Ford shale.

3.1 Facies A

As mentioned in Section 2 some samples were damaged after the initial experiment and we could not run the three different (unpropped, 100 mesh and 30/50) experiments with them. For this reason the surface attributes have to be calculated for each set of experiments to only include the samples that were used at each conditions. This point is illustrated on Table. 3.1. The same procedure was followed for the other four geological facies.

Table. 3.1 – Surface Attributes for the Different Experimental Conditions-Facies A.

Zone A-Unpropped	R_{RMS} ,in	Fracture Area, in^2	Number of Data Points
X0	0.24	9.42	2
X90	0.21	9.27	2
X0 & X90 Average	0.22	9.35	4
Zone A-100 mesh	R_{RMS} ,in	Fracture Area, in^2	Number of Data Points
X0	0.20	9.24	1
X90	0.21	9.27	2
X0 & X90 Average	0.20	9.26	3
Zone A-30/50 mesh	R_{RMS} ,in	Fracture Area, in^2	Number of Data Points
X0	--	--	0
X90	0.23	9.45	1
X0 & X90 Average	0.23	9.45	1

3.1.1 Unpropped Fracture Conductivity Facies A

Facies A is formed by interbedded light grey grainstones and mudstones (Donovan et al. 2012). In general the interface between two different sedimentary layers behave as a weak plane (Peng and Zhang 2007). Our samples contained weak planes on the fracture face that were broken as the closure stress was applied. These planes broke into little pieces of rocks that enhanced the unpropped fracture conductivity of Facies A. The unpropped fracture conductivity with the fracture area and surface roughness for each sample for facies A are presented on **Fig. 3.1**.

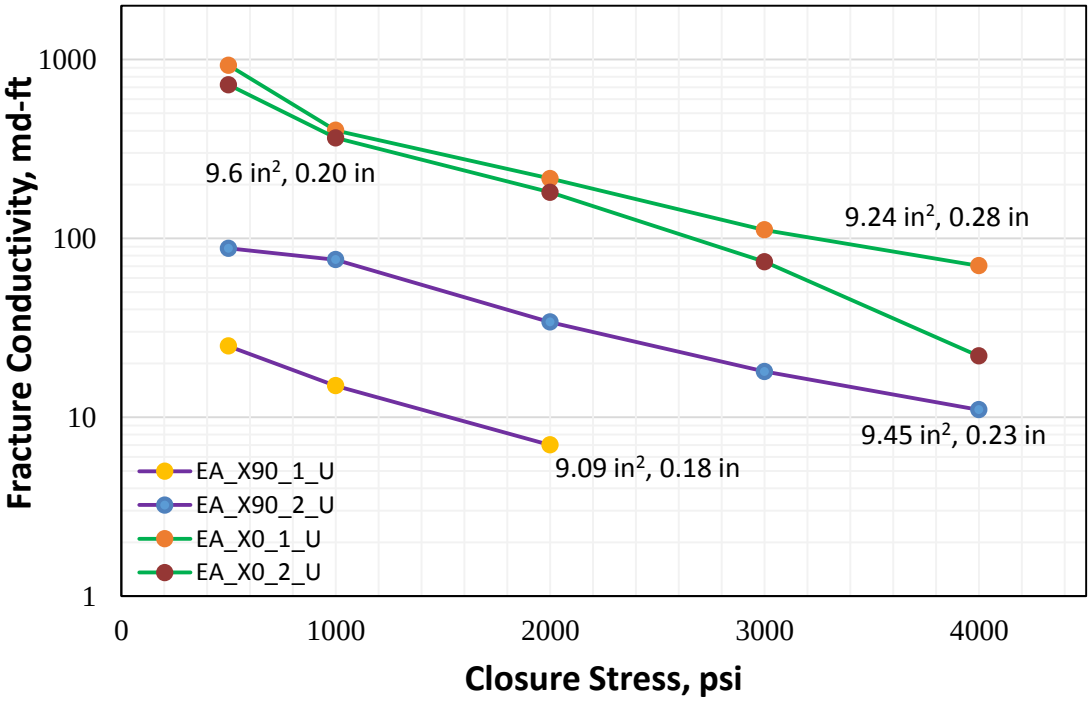

Fig. 3.1 – Unpropped Fracture Conductivity, Fracture Area and Roughness- Facies A.

The failure of weak plans located in the fracture face was evident for samples EA_X0_1_U and EA_X0_2_U (**Fig. 3.2**). This dominates the conductivities for these two samples and explains their high values. For samples in the X90 direction we can see that a greater fracture area increases the conductivity by decreasing the effective closure stress in the fracture face and becomes more important as closure stress increases. The final observation for the unpropped fracture conductivity of Facies A is that it declines exponentially as closure stress increases (**Fig. 3.3**).

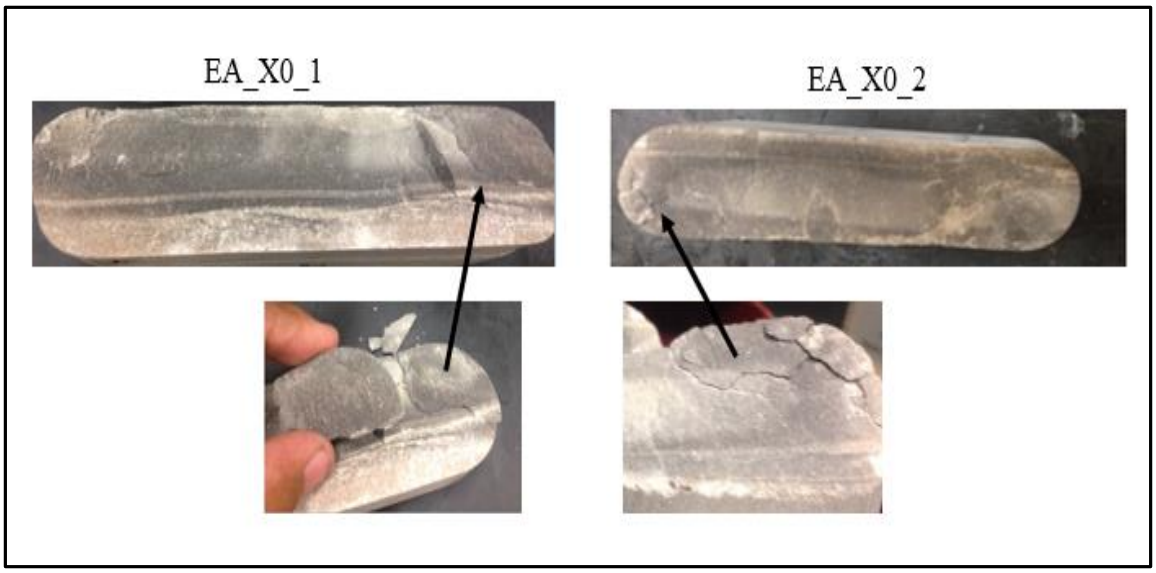

Fig. 3.2 – Samples EA_X0_1 and EA_X0_2 Weak Planes in the Fracture Faces.

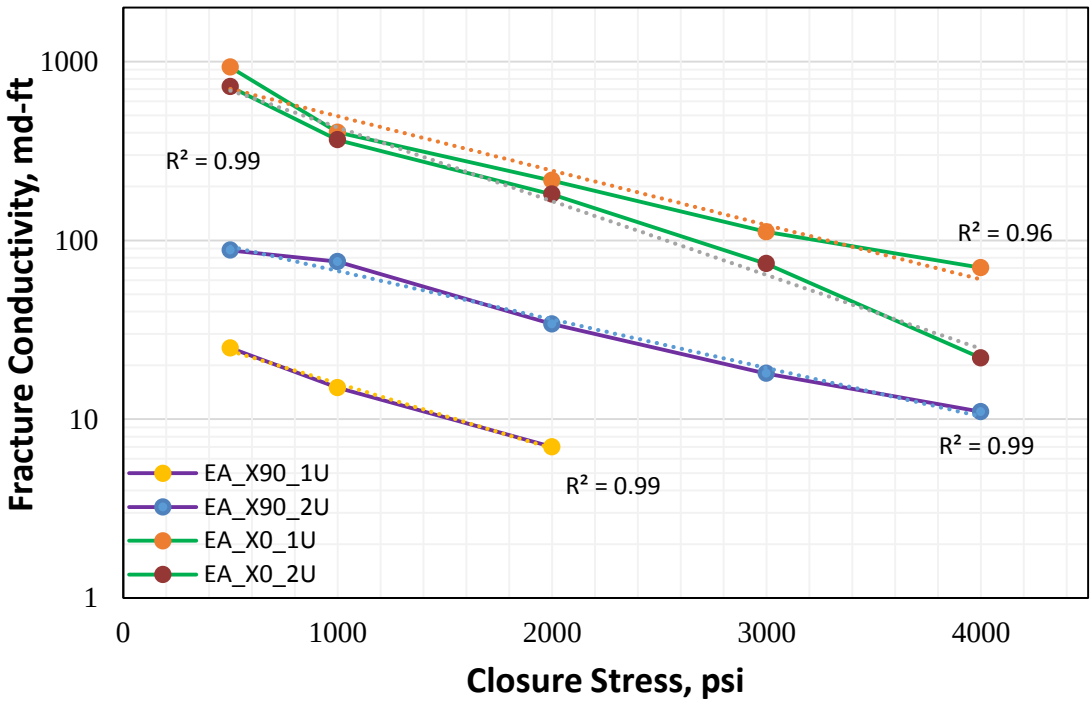

Fig. 3.3 – Exponential Decline of Unpropped Fracture Conductivity-Facies A.

3.1.2 Propped Fracture Conductivity Facies A

The propped fracture conductivity with the fracture area and surface roughness for each sample for facies A is displayed in **Fig. 3.4** for 100 mesh-0.1 lbm/ft^2. The following conclusions can be drawn from this plot: greater fracture area leads to higher conductivity at high closure stress. Higher roughness correlates with high conductivities at low closure stress. Propped conductivity declines exponentially with closure stress as can be seen by the R^2 values obtained with an exponential fit.

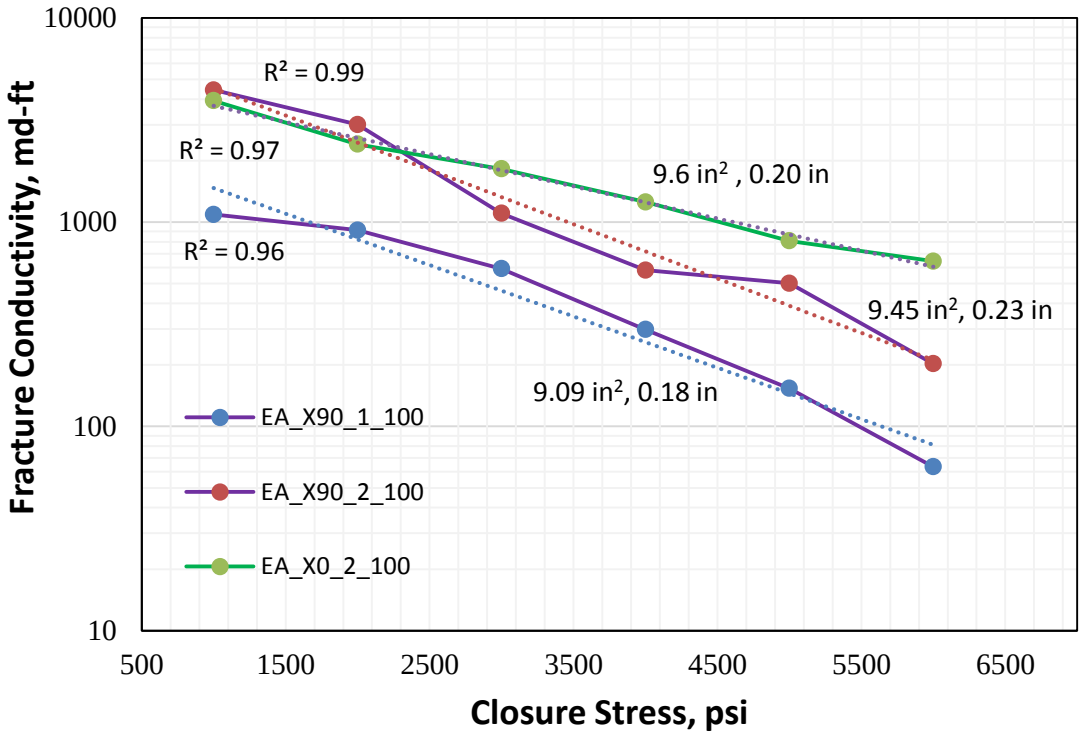

Fig. 3.4 – 100 Mesh-0.1 lbm/ft^2 Fracture Conductivity, Fracture Area and Roughness-Facies A.

After performing the 100 mesh experiment only one sample (EA_X90_2) was in good condition to run the 30/50 mesh experiment. The difference between unpropped and propped fracture conductivity is almost two orders of magnitude. For the used concentration 100 mesh and 30/50, the conductivities are almost identical at closure stresses below 2000 psi, after this point the conductivity with 30/50 mesh proppant is better maintained than the one generated with the 100 mesh proppant (**Fig. 3.5**).

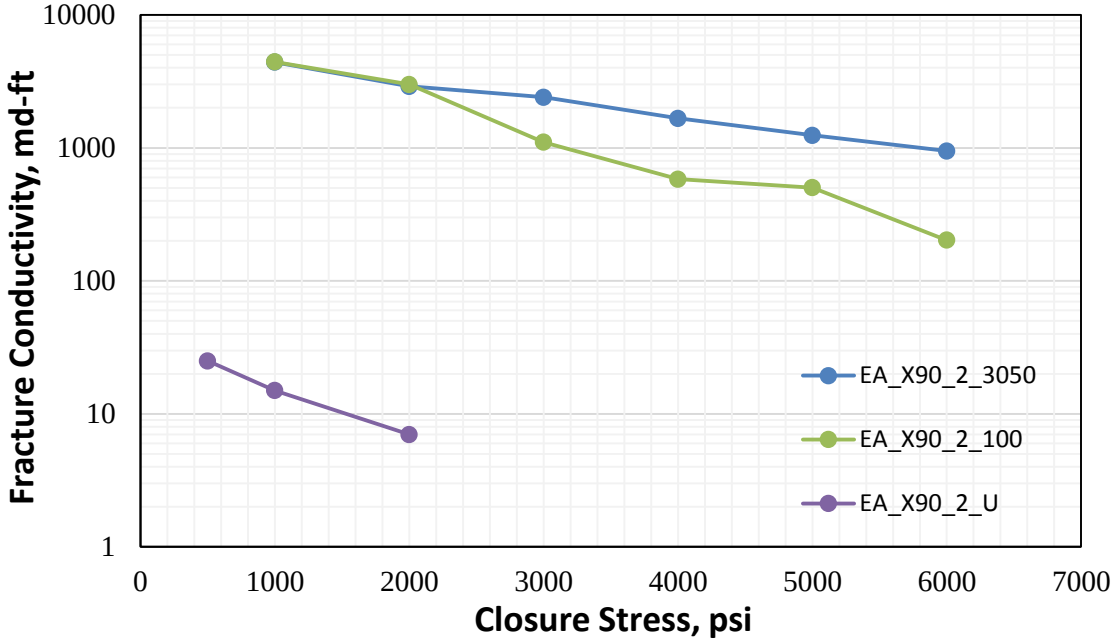

Fig. 3.5 – 30/50 Mesh-0.1 lbm/ft^2, 100 mesh-0.1 lbm/ft^2 and Unpropped Fracture Conductivity- Sample: EA_X90_2.

3.2 Facies B

Facies B is the zone with the highest total organic content and production. For this reason more samples were obtained from this zone. This is the only zone where flow on the bedding plane was analyzed (Z direction). A summary of the experiments and surface attributes of the samples from facies B is presented in Table. 3.2. The samples obtained from facies B were gray to black in color with no distinctive bedding planes on them (**Fig. 3.6**).

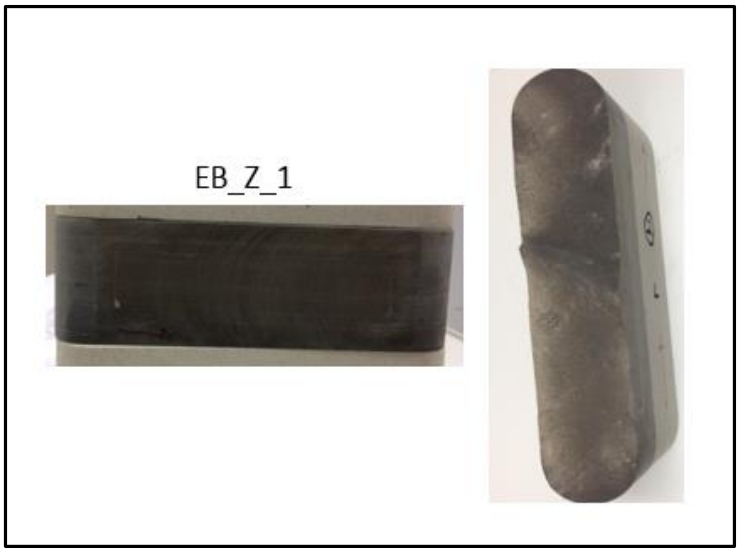

Fig. 3.6 – Facies B: Dark to Gray Samples-Sample: EB_Z_1.

Table. 3.2 – Surface Attributes for the Different Experimental Conditions-Facies B.

Zone B-Unpropped	R_{RMS}, in	Fracture Area, in^2	Number of Data Points
X0	0.21	10.34	2
X90	0.26	9.27	2
X0 & X90 Average	0.23	9.35	4
Z	0.17	9.06	3
Zone B-100 mesh	R_{RMS}, in	Fracture Area, in^2	Number of Data Points
X0	0.14	9.68	3
X90	0.25	9.21	4
X0 & X90 Average	0.20	9.41	7
Z	0.18	9.04	3
Zone B-30/50 mesh	R_{RMS}, in	Fracture Area, in^2	Number of Data Points
X0	0.17	10.72	1
X90	0.25	9.21	3
X0 & X90 Average	0.23	9.59	4
Z	0.20	9.03	1

3.2.1 Unpropped Fracture Conductivity Facies B

The following observations can be made based on the results obtained in facies B. In general, unpropped fracture conductivity was dominated by the surface area at high closure stress and by the surface roughness (R_{Rms}) at low closure stress. The conductivity declines exponentially as closure stress increases (**Fig. 3.7**). It is important to note that the increase in surface area and roughness also have the negative effect on conductivity of increasing the flow path length. For some samples or at some specific conditions, this negative effect may overtake the positive effects created by the "channels" from the contact of two rough surfaces and the lower effective stress due to a greater surface area. This may explain some of the deviation of conductivity behavior from the expected results.

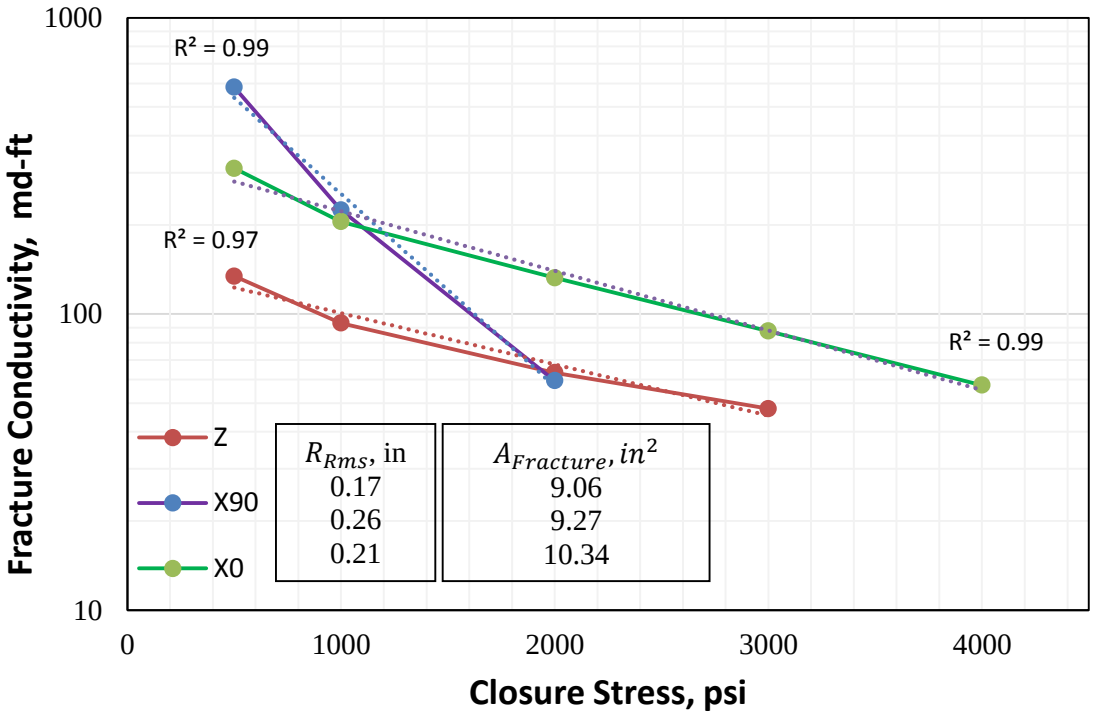

Fig. 3.7 – Average Unpropped Fracture Conductivity, Exponential Decline Trend line and Fracture Area and Roughness- Facies B.

3.2.2 Propped Fracture Conductivity Facies B

The propped fracture conductivity for facies B exhibit similar trends to the unpropped conductivity for this zone. A high surface roughness is linked to high conductivity, at low closure stress, and a high fracture area helps maintain the conductivity at high closure stress. There is not a clear point where the surface roughness, fracture area and/or the negative effect from these parameters (longer flow path) dominate. Propped conductivity declines exponentially with closure stress. The same trends were seen for both the 100 Mesh- 0.1 lbm/ft^2 experiments (**Fig. 3.8**) and the 30/50 Mesh- 0.1 lbm/ft^2 experiments (**Fig. 3.9**). The unpropped fracture conductivity was at least an order of magnitude lower than the propped conductivity, the difference increases as closure stress increase. For the concentrations used, 30/50 mesh proppant has a higher conductivity than 100 mesh proppant. However, the difference decreases as the closure stress increases and at 6,000 psi of closure stress, it is negligible (**Fig. 3.10**).

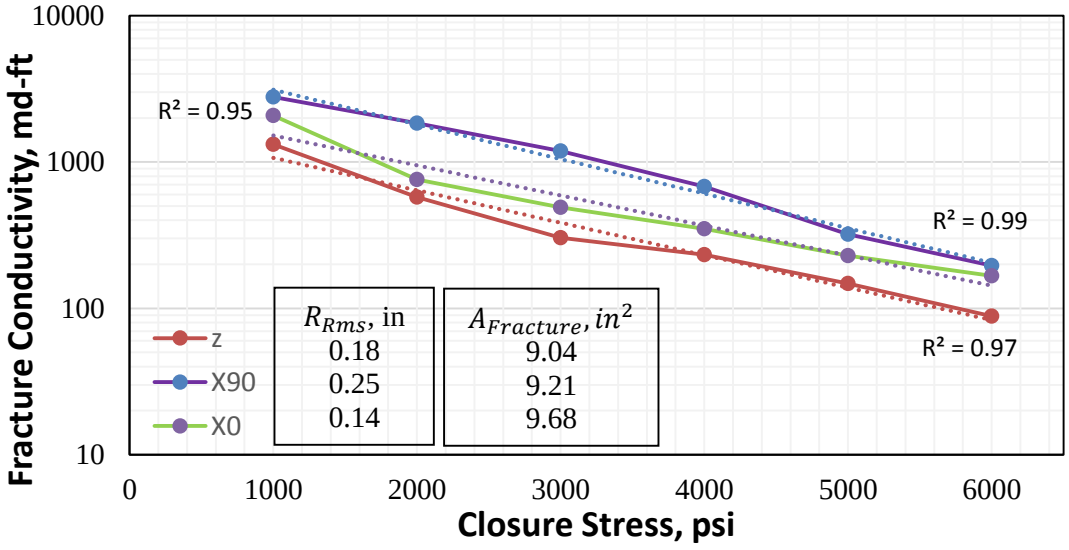

Fig. 3.8 – 100 Mesh-0.1 lbm/ft^2 Fracture Conductivity, Exponential Decline Trend Line and Fracture Area and Roughness- Facies B.

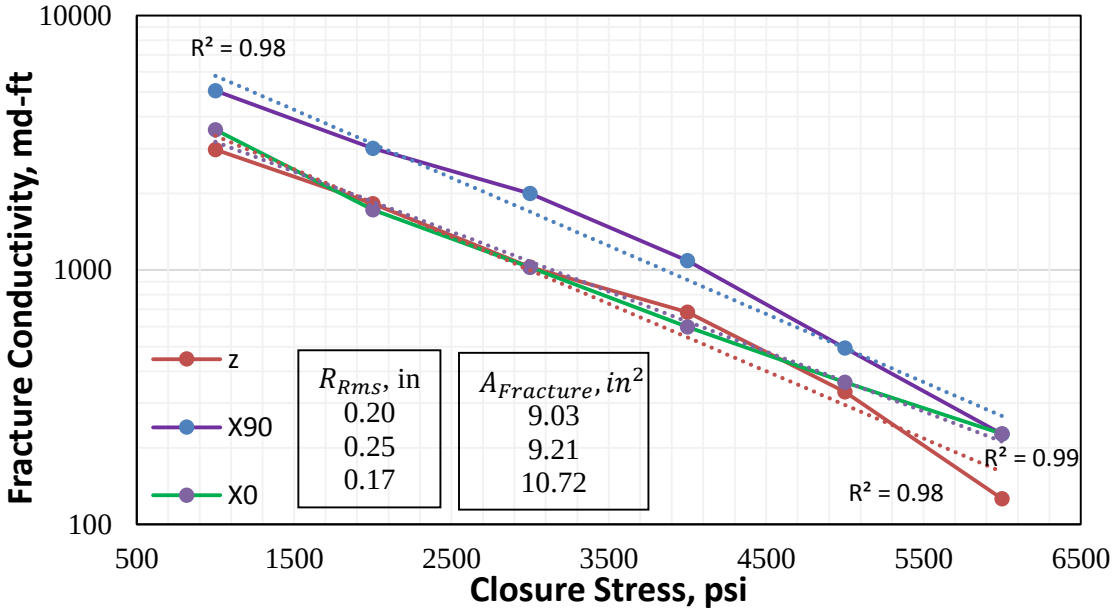

Fig. 3.9 – 30/50 Mesh- 0.1 lbm/ft^2 Fracture Conductivity, Exponential Decline Trend Line and Fracture Area and Roughness- Facies B.

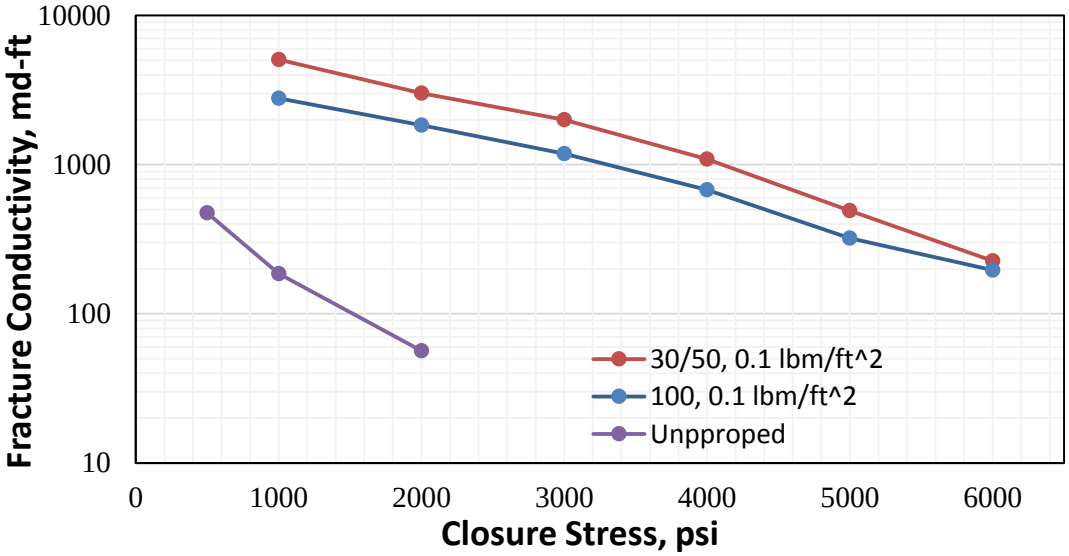

Fig. 3.10 – 30/50 Mesh-0.1 lbm/ft^2, 100 Mesh- 0.1 lbm/ft^2 and Unpropped Fracture Conductivity X90 Direction- Facies B.

3.3 Facies C

Facies C is the first zone in the upper Eagle Ford shale. Samples from this zone are in between the dark color obtained from facies B and the light-yellowish found in facies D (**Fig. 3.11**). A summary of the experiments and surface attributes of the samples from facies C is presented in Table. 3.3.

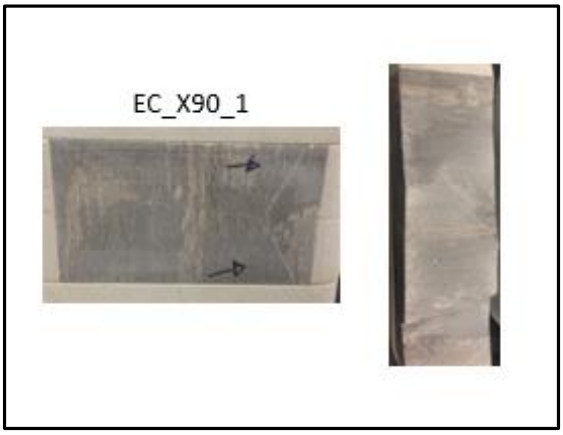

Fig. 3.11 – Facies C-Sample EC_X90_1.

Table. 3.3 – Surface Attributes for the Different Experimental Conditions-Facies C.

Zone C-Unpropped	R_{RMS}, in	Fracture Area, in^2	Number of Data Points
X0	0.08	9.24	1
X90	--	--	0
X0 & X90 Average	0.08	9.24	1
Zone C-100 mesh	R_{RMS}, in	Fracture Area, in^2	Number of Data Points
X0	0.15	9.38	2
X90	0.18	9.37	2
X0 & X90 Average	0.16	9.37	4
Zone C-30/50 mesh	R_{RMS}, in	Fracture Area, in^2	Number of Data Points
X0	--	--	0
X90	0.17	9.28	1
X0 & X90 Average	0.17	9.28	1

3.3.1 Unpropped Fracture Conductivity Facies C

Only one unpropped experiment was performed in Facies C. The conductivity declines exponentially as closure stress increases (**Fig. 3.12**).

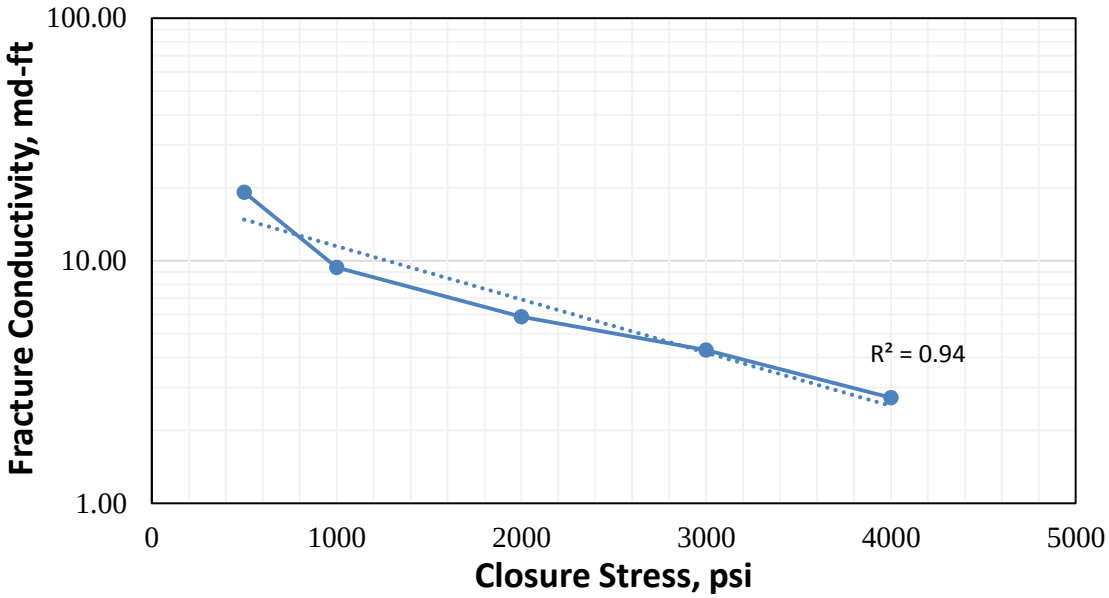

Fig. 3.12 – Unpropped Fracture Conductivity Sample: EC_X90_1-Facies C.

3.3.2 Propped Fracture Conductivity Facies C

The same general trends observed in Facies A and B are present in facies C. Samples with high surface roughness tend to have a higher initial conductivity than samples with smooth surfaces. Fracture area helps maintain the conductivity at high closure stress. Conductivity declines exponentially with closure stress (**Fig. 3.13**). For the concentrations used, 30/50 mesh proppant creates a higher conductivity than the one from 100 mesh proppant. The difference between the conductivities declines as stress increases and at 6,000 psi of

closure stress the conductivities are pretty much equal. Unpropped conductivities are about two orders of magnitude smaller than propped conductivities (**Fig. 3.14**).

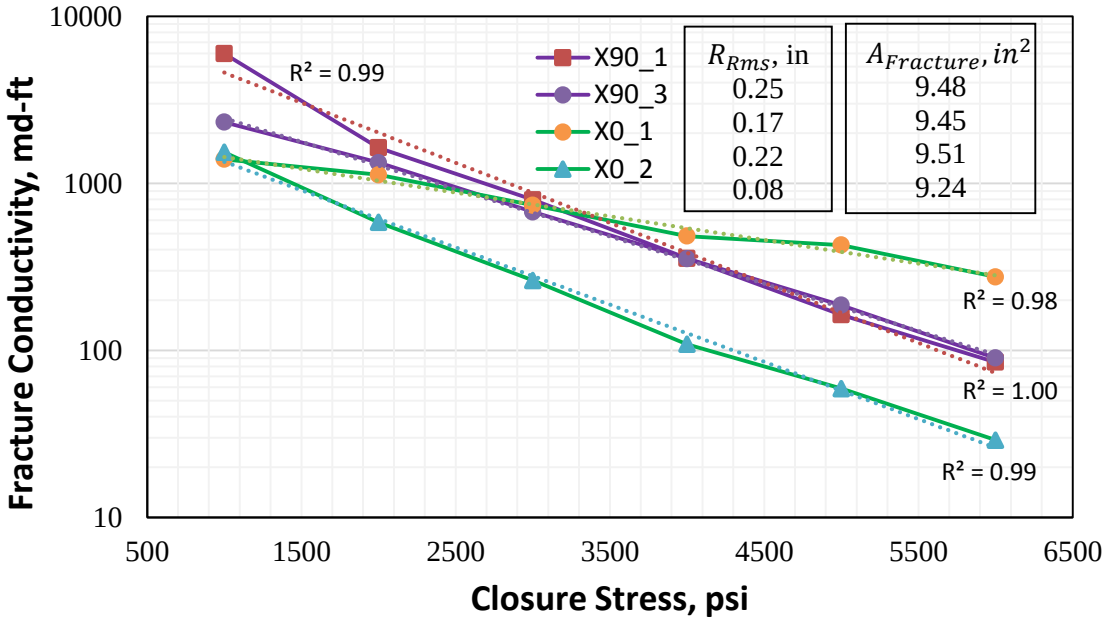

Fig. 3.13 – 100 Mesh-0.1 lbm/ft^2 Fracture Conductivity, Exponential Decline Trend Line and Fracture Area and Roughness-Facies C.

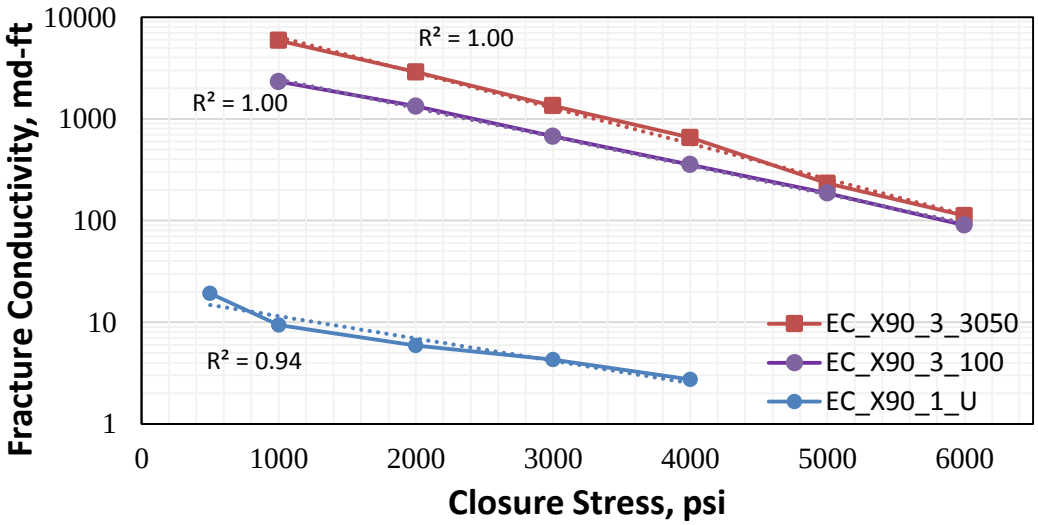

Fig. 3.14 – 30/50 Mesh- 0.1 lbm/ft^2,100 Mesh- 0.1 lbm/ft^2 and Unpropped Fracture Conductivity-Facies C.

3.4 Facies D

The samples obtained from facies D are lighter in color than the ones obtained from facies C. The mineralogy and appearance of facies D are closer to the mineralogy and appearance of facies E than to the rest of the Eagle Ford shale (**Fig. 3.15**). A summary of the experiments and surface attributes of the samples from facies D is presented in Table. 3.4.

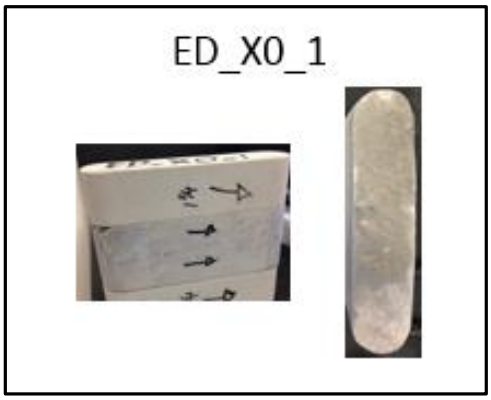

Fig. 3.15 – Facies D-Sample ED_X0_1.

Table. 3.4 – Surface Attributes for the Different Experimental Conditions-Facies D.

Zone D-Unpropped	R_{RMS}, in	Fracture Area, in^2	Number of Data Points
X0	0.27	9.53	2
X90	0.26	9.37	1
X0 & X90 Average	0.26	9.47	3
Zone D-100 mesh	R_{RMS}, in	Fracture Area, in^2	Number of Data Points
X0	0.27	9.53	2
X90	0.28	9.45	2
X0 & X90 Average	0.27	9.49	4
Zone D-30/50 mesh	R_{RMS}, in	Fracture Area, in^2	Number of Data Points
X0	0.28	9.77	1
X90	0.29	9.53	1
X0 & X90 Average	0.29	9.65	2

3.4.1 Unpropped Fracture Conductivity Facies D

The unpropped fracture conductivity for facies D does not follow the relationships between the surface attributes and fracture conductivity previously observed in faces A, B and C. Visually, there is no difference between the X0 and X90 samples for zone D. It is possible that the mechanical properties of the sample in the X90_2 (local heterogeneity) are different than the ones from the other samples and that these properties dominate the conductivity behavior. The conductivity declines exponentially with closure stress (**Fig. 3.16**).

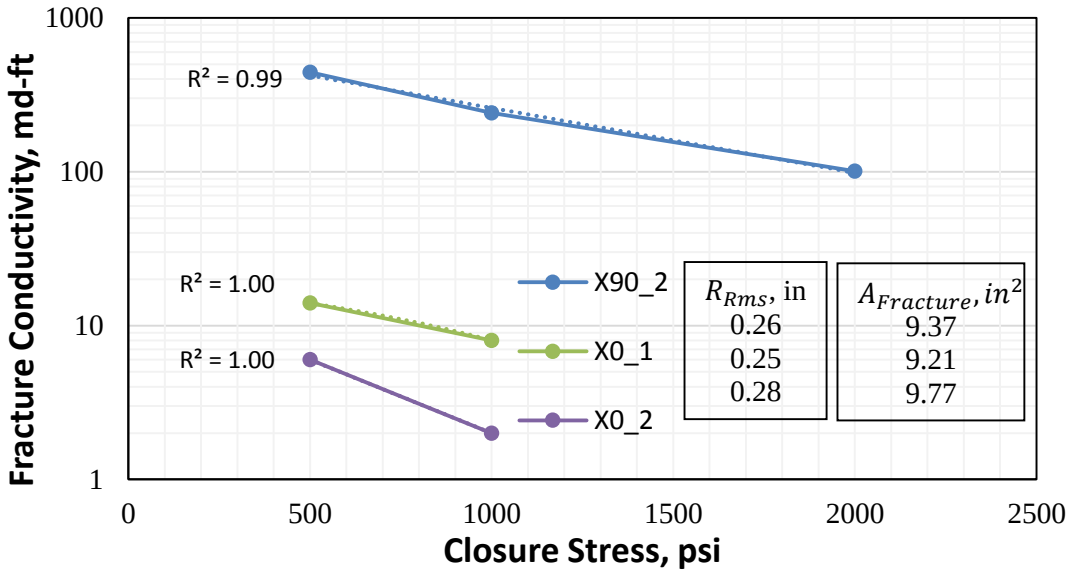

Fig. 3.16 – Unpropped Fracture Conductivity, Exponential Decline Trend Line Fracture Area and Roughness- Facies D.

3.4.2 Propped Fracture Conductivity Facies D

The surface attributes do not have the positive relationship previously (Facies A, B and C) observed with fracture conductivities at low closure stress. Having said that, the values of roughness for this zone are very close together, and so are the values of conductivity at

low closure stress. In addition to this, the sample with the lowest fracture area has the lowest conductivity at 6,000 psi of closure stress. The conductivity declines exponentially with closure stress (**Fig. 3.17**). For the concentrations used, 30/50 mesh proppant creates a slightly higher conductivity than the one from 100 mesh proppant. The difference between these conductivities is not as great as in facies A, B and C. The propped conductivity is more than two orders of magnitude greater than unpropped conductivity (**Fig. 3.18**). It seems that the properties of the rock are playing a considerable role in the conductivity of facies D.

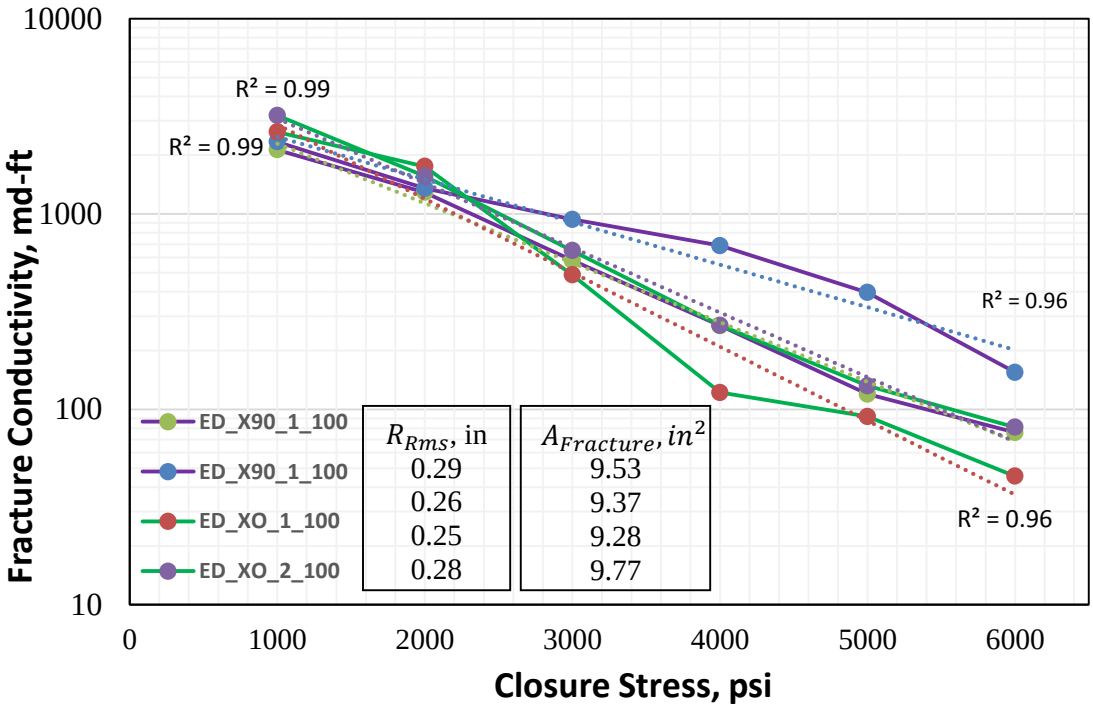

Fig. 3.17 – 100 Mesh-0.1 lbm/ft^2 Fracture Conductivity, Exponential Decline Trend Line and Fracture Area and Roughness- Facies D.

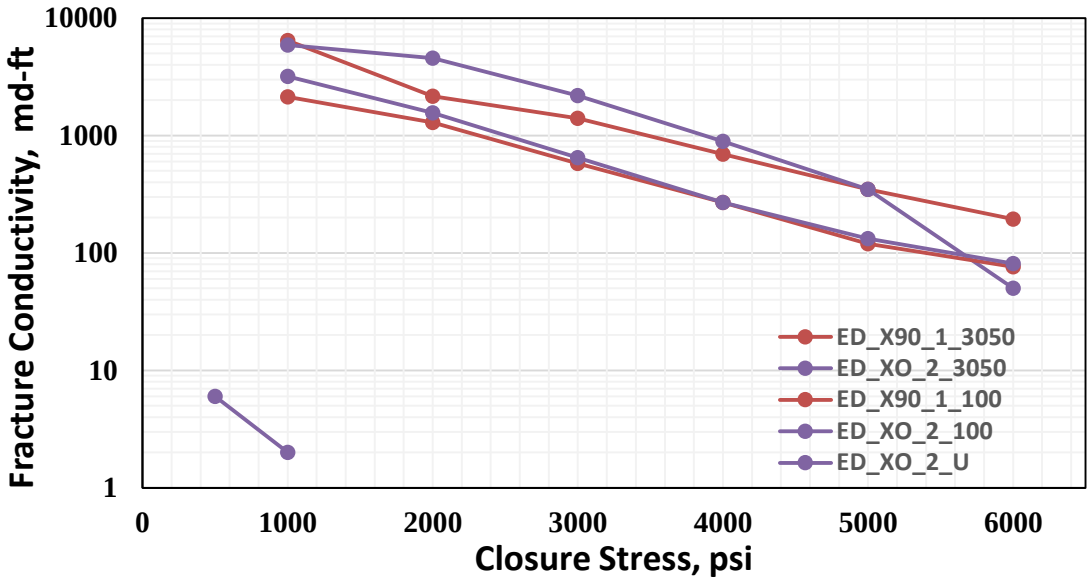

Fig. 3.18 – 30/50 Mesh-0.1 lbm/ft^2, 100 Mesh- 0.1 lbm/ft^2 and Unpropped Fracture Conductivity- Facies D.

3.5 Facies E

Facies E is light colored and closer to facies D than to the other facies of the Eagle Ford shale. Different bedding planes can be seen in samples from this facies (**Fig. 3.19**). A summary of the experiments and surface attributes of the samples from facies E is presented in Table. 3.5.

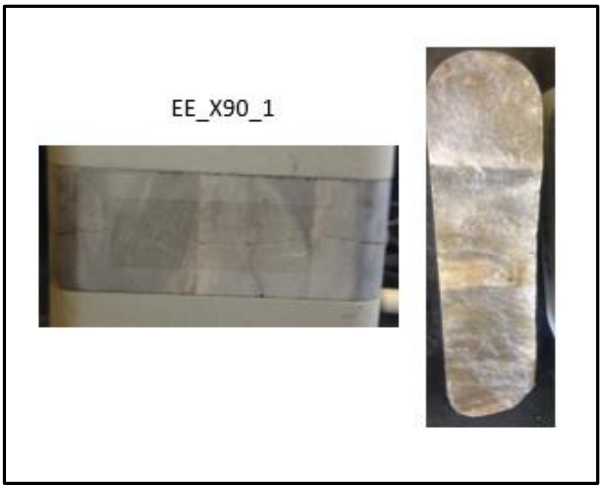

Fig. 3.19 – Facies E-Sample EE_X90_1.

Table. 3.5 – Surface Attributes for the Different Experimental Conditions-Facies E.

Zone E-Unpropped	R_{RMS}, in	Fracture Area, in^2	Number of Data Points
X0	0.18	9.03	1
X90	0.21	9.37	2
X0 & X90 Average	0.20	9.26	3
Zone E-100 mesh	R_{RMS}, in	Fracture Area, in^2	Number of Data Points
X0	0.21	9.30	2
X90	0.21	9.37	2
X0 & X90 Average	0.21	9.33	4
Zone E-30/50 mesh	R_{RMS}, in	Fracture Area, in^2	Number of Data Points
X0	0.21	9.30	2
X90	0.2	9.48	1
X0 & X90 Average	0.20	9.36	3

3.5.1 Unpropped Fracture Conductivity Facies E

There is no trend between the surface attributes and the unpropped fracture conductivity. This is consistent with the results obtained in facies D. The mechanical properties or the heterogeneities (**Fig. 3.20**) of the samples may be dominating the conductivity. The mechanical properties and mineralogy for the facies were measured from core plugs obtained from the same rocks where the conductivity samples were obtained and not from

the actual conductivity samples. For this reason it is not possible to use these properties to compare experiments within the same facies. The conductivity declines exponentially with the closure stress.

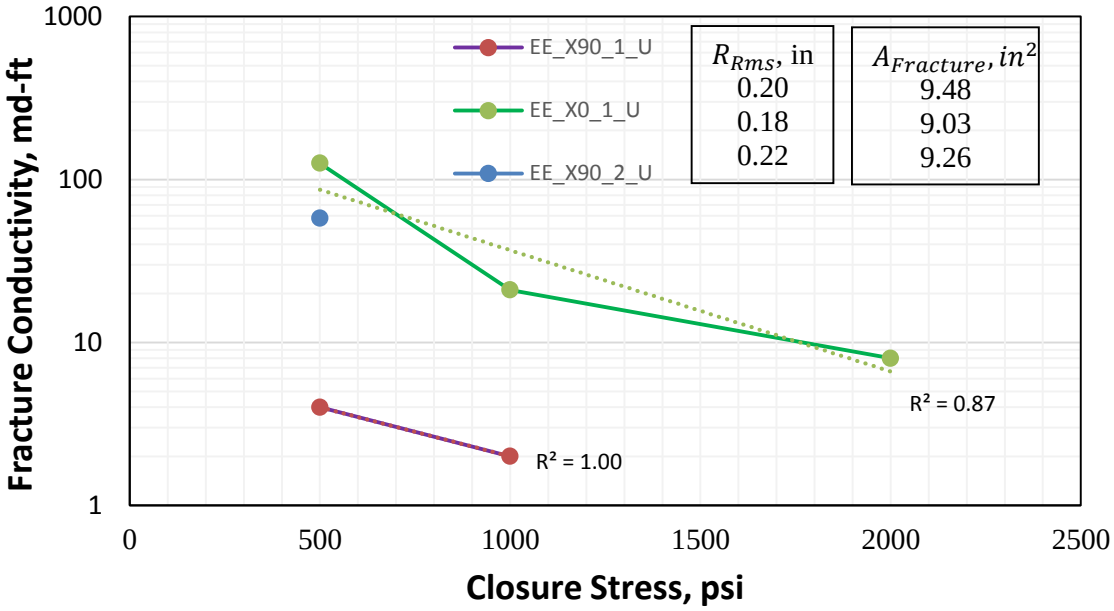

Fig. 3.20 – Unpropped Fracture Conductivity, Exponential Decline Trend Line Fracture Area and Roughness-Facies E.

3.5.2 Propped Fracture Conductivity Facies E

There is not an apparent relationship between the propped fracture conductivity and the surface attributes for facies E (**Fig. 3.21**). For the concentration used in this study the conductivity obtained with the 30/50 mesh proppant is significantly higher than the one obtained with the 100 mesh proppant (**Fig. 3.22**). The propped conductivity is more than two orders of magnitude higher than the unpropped conductivity (**Fig. 3.23**). Both propped and unpropped conductivity decline exponentially with closure stress.

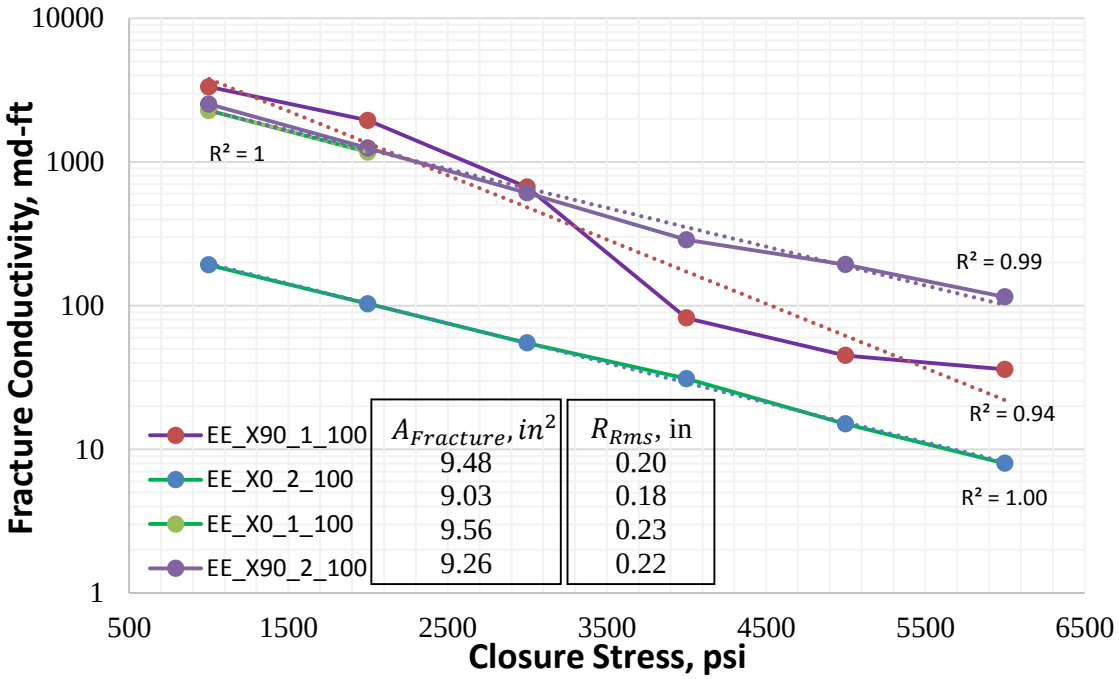

Fig. 3.21 – 100 Mesh-0.1 lbm/ft^2 Fracture Conductivity, Exponential Decline Trend Line and Fracture Area and Roughness-Facies E.

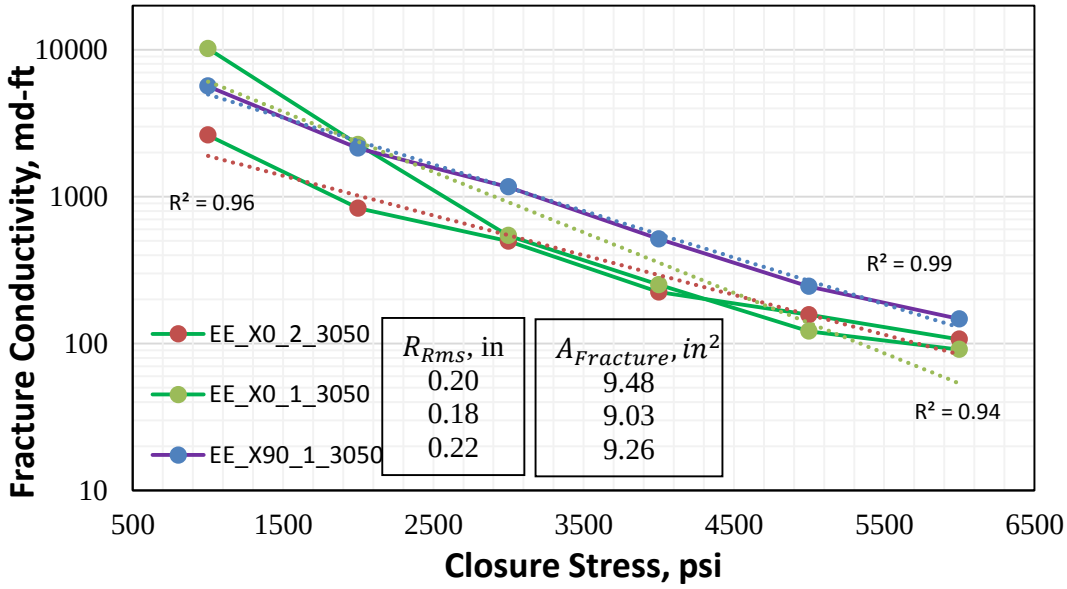

Fig. 3.22 – 30/50 Mesh-0.1 lbm/ft^2 Fracture Conductivity, Exponential Decline Trend Line and Fracture Area and Roughness-Facies E.

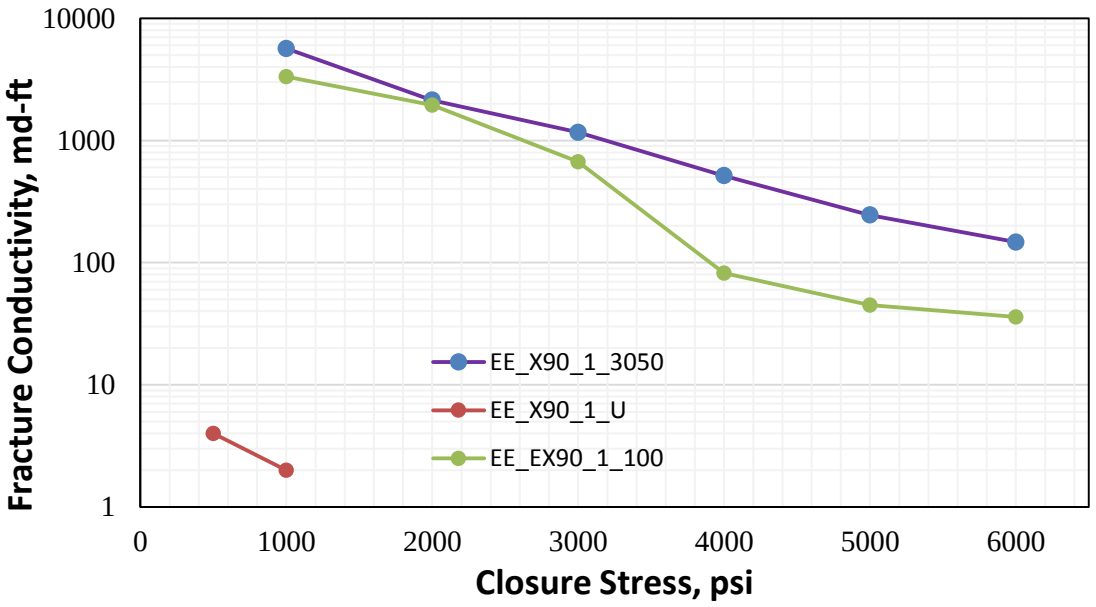

Fig. 3.23 – 30/50 Mesh- 0.1 lbm/ft^2, 100 Mesh- 0.1 lbm/ft^2 and Unpropped Fracture Conductivity- Facies E.

4. FRACTURE CONDUCTIVITY COMPARISONS ACROSS FACIES A-E

Fracture conductivity for all five Eagle Ford zones are cross examined in this section. The effect of mechanical properties, fracture orientation and mineralogy on conductivity is discussed.

4.1 Fracture Conductivity Orientation

The impact of fracture orientation is analyzed for the results obtained for the 100 mesh-0.1 lbm/ft^2, the conditions with the most number of experiments. Unpropped conductivity was not used for this purpose due to small number of completed experiments. Furthermore, for some facies unpropped experiments are only available in one direction. The fracture conductivities for the X0 and X90 for facies A,B C can be seen In **Fig. 4.1** and for facies D and E In **Fig. 4.2**.

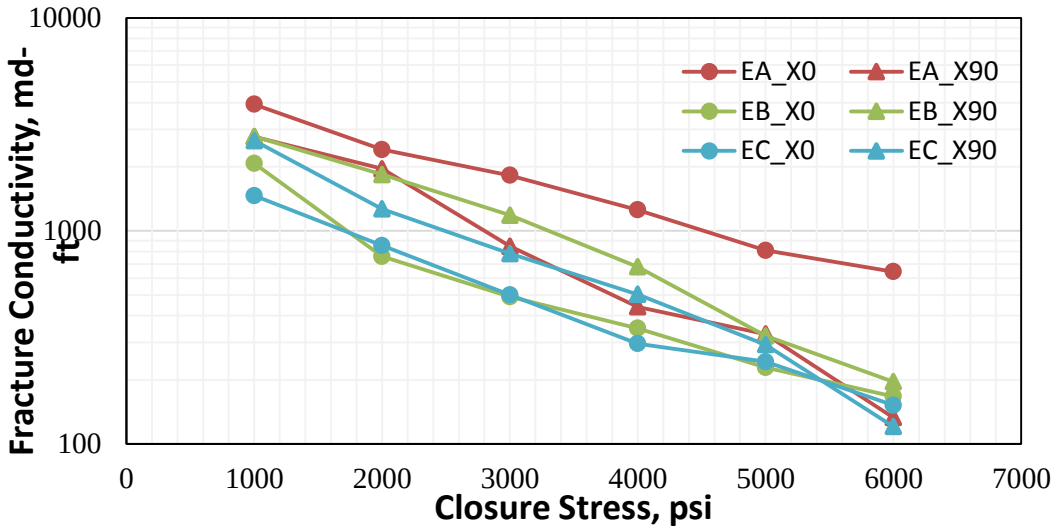

Fig. 4.1 – Fracture Conductivity for 100 Mesh-0.1 lbm/ft^2 Concentration in the X0 and X90 Directions for Facies A, B and C.

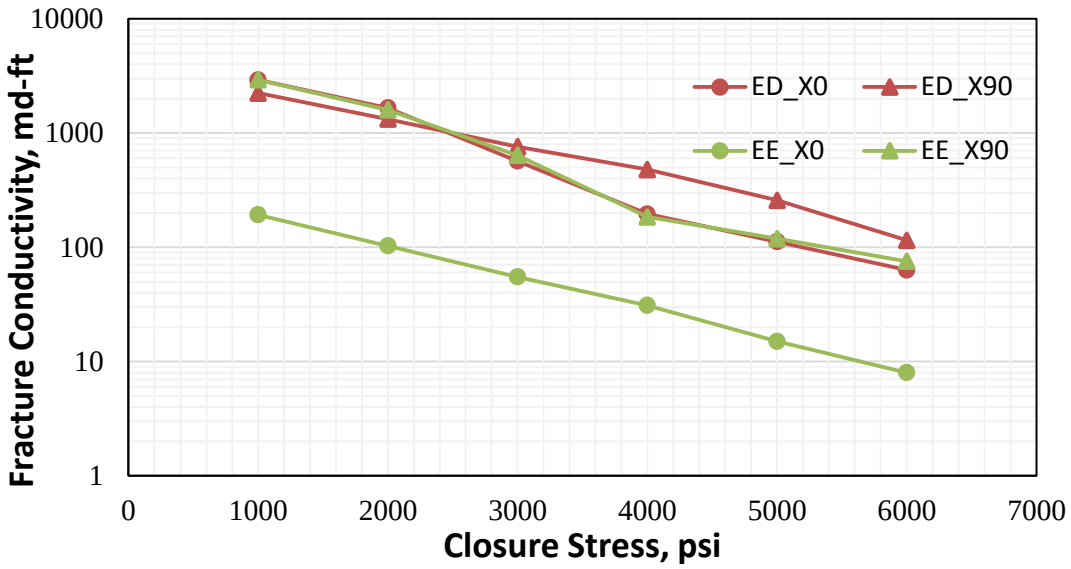

Fig. 4.2 – Fracture Conductivity for 100 Mesh-0.1 lbm/ft^2 Concentration in the X0 and X90 Directions for Facies D and E

There is no trend of fracture orientation effect between the X0 and X90 directions across the five geological facies. At low closure stresses in facies A, the conductivity of samples in the X0 direction is greater than the conductivity of samples in the X90 direction. The same can be said for facies D. Facies B, C and E show the opposite trend, where the conductivity in the X90 direction is greater than the one in the X0 direction. At high closure stress, the conductivity in X0 and X90 have similar values for facies B,C and D. In facies A, there is a big difference between the X0 and X90 direction at high closure stress which may be caused by weak planes in the fracture face (**Fig. 3.2)**. Facies E shows a significant difference (at low and high closure stress) between X0 and X90, possible causes for this were discussed in section 3.5.2.

Samples in the Z direction (along the bedding plane) tend to break relatively easy along the bedding plane which result in smoother fractures with less surface area than samples

in the X0 and X90 direction. These surface attributes could explain the lower fracture conductivity of samples in the Z direction compared to samples in the X0 and X90 direction (**Fig. 4.3)**.

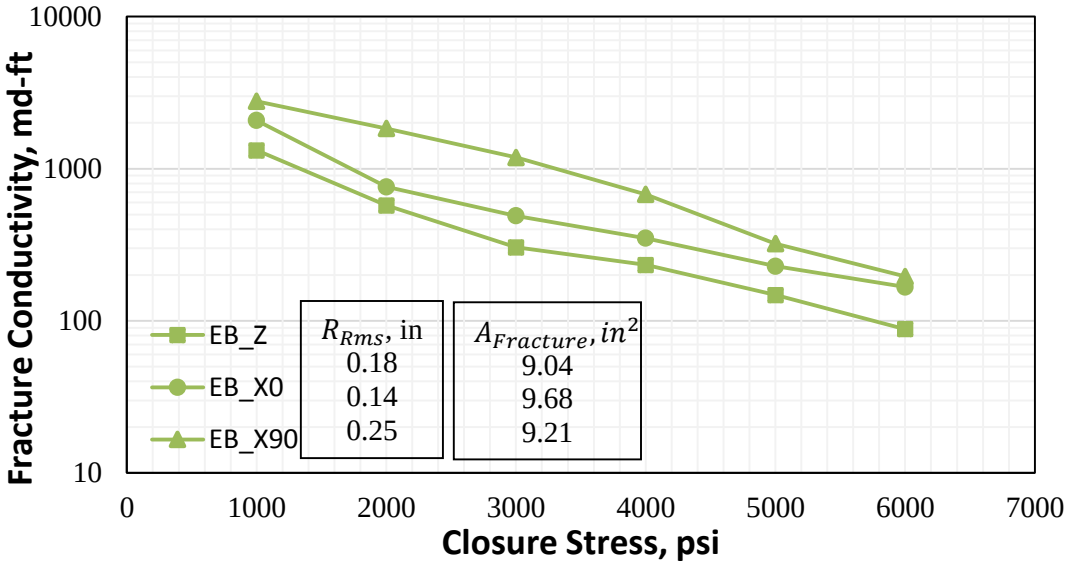

Fig. 4.3 – Fracture Conductivity for 100 Mesh 0.1 lbm/ft^2 Concentration Facies B: Samples in Z, X0 and X90 Directions and Fracture Area and Roughness.

4.2 Mechanical Properties and Brittleness Index

The mineralogy and total organic content (TOC) presented in Section 2 are used in this section. The mechanical properties were experimentally (triaxial and Brinell test) determined by Knorr (2016) from the core plugs (1 inch in diameter by 2 inches in length) obtained from the same rocks where the conductivity samples were obtained. The nomenclature for the core plug's name is the following: formation name (E), geological facies (A-E), followed by a dash and the sample orientation. Where X means that the

loading was made parallel to the bedding planes and Z means that it was made perpendicular to the bedding planes. For example, sample EA-X is a core plug from the Eagle Ford shale obtained from facies A and the mechanical properties were measured by applying load parallel to the bedding planes. The conductivity samples in the X0 and X90 correspond to the X direction samples and our Z direction correspond to the Z direction in the nomenclature used by Knorr (2016). A summary of the mechanical properties can be seen in Table. 4.1.

Table. 4.1 – Summary of the Mechanical Properties: Young's Modulus, Poisson's Ratio and Brinell Hardness for the Eagle Ford Shale Samples.

	E,psi	***v***	**Brinell Hardness Number (kgf/mm2)**	**Number of Samples**
EA-X	3.98E+06	0.151	92	3
EB-X	4.06E+06	0.164	113	6
EB-Z	3.52E+06	0.140	96	6
EC-X	3.78E+06	0.178	82	3
ED-X	4.82E+06	0.191	92	2
EE-X	5.01E+06	0.213	91	3

Brittleness index was calculated based on the mineralogy and total organic content (**Eq. 3-1**) with the equation presented by Wang and Gale (2010). The following process was repeated for the five different geological facies:

$$BI_{Mi} = \frac{Q+Dol}{(Q+Dol+Lm+Cl+TOC)} \quad \text{(3-1)}$$

Where Q is the quartz, Dol is dolomite, Lm is limestone (calcite), Cl is the total amount of clays and TOC is the total organic content in the sample. The brittleness indexes calculated from the mineralogy and total organic content are presented in Table. 4.2.

Table. 4.2 – Brittleness Index for the Eagle Ford Shale Samples.

Facies	BI_{Mi}
EA_X	0.11
EB_X	0.19
EB_Z	0.19
EC_X	0.12
ED_X	0.03
EE_X	0.06

As discussed in section 4.1 we found no significant difference between samples oriented in the X0 and X90 direction. For this reason and in order to have a greater number of samples to compare the conductivities across the five different geological facies, an average of X0 and X90 samples was obtained. The average is represented as X. The results for the 100 mesh 0.1 lbm/ft^2 concentration are shown in **Fig. 4.4**.

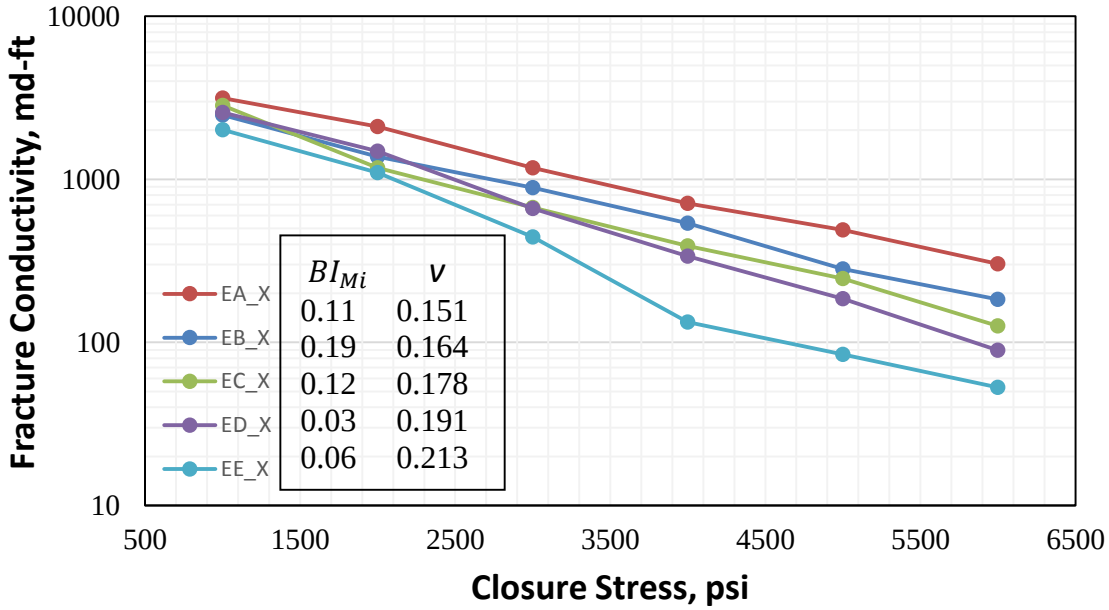

Fig. 4.4 – Fracture Conductivity Facies A-E and Brittleness Indexes. 100 Mesh- 0.1 lbm/ft^2 Concentration.

At low closure stress the average conductivities for the five different geological facies are very close together. For this reason it seems that the proppant is dominating the conductivity at this stage. As the stress increases, the difference in the conductivities also increases. It seems that facies with high brittleness and low Poisson's Ratio are able to maintain the fracture conductivity better than those with low brittleness and high Poisson's Ratio. For facies A, the failure of weak planes located in the fracture face seem to dominate the conductivity and explains their high values (**Fig. 3.2**). It is important to consider that facies C has the lowest Brinell hardness and facies B has the highest Brinell hardness. The BI_{Mi} of facies E is greater than the one from facies D but the conductivity of facies E is less than the one obtained from facies D. Visually, samples from facies E have the most heterogeneities (bedding planes on samples) which could explain the discrepancy. For

these reasons it is not possible to affirm that brittleness is the dominating factor of fracture conductivity, however, there seems to be a positive correlation between brittleness and fracture conductivity. From the brittleness index it is clear that there is a significant difference between facies E and D and the rest of the Eagle Ford shale. This is consistent with observation made by Donovan et al. (2012) where it was pointed out that facies E and D are closer to the Austin Chalk than to the rest of the Eagle Ford shale. Furthermore, it supports the analysis made in sections 3.5.1 and 3.5.2. There is no trend of Young's Modulus and Brinell hardness (Table. 4.2) effect and fracture conductivity. Poisson's Ratio seems to be inversely related to fracture conductivity.

The same process was applied for the 30/50 mesh-0.1 lbm/ft^2 (**Fig. 4.5**) concentration. Similar trends can be seen for this condition, however, there are less samples available at these concentrations (Table. 4.3) and the 30/50 mesh experiments were performed after the unpropped and 100 mesh experiments. There is a possibility that the rocks were weakened by multiple stress loading cycles.

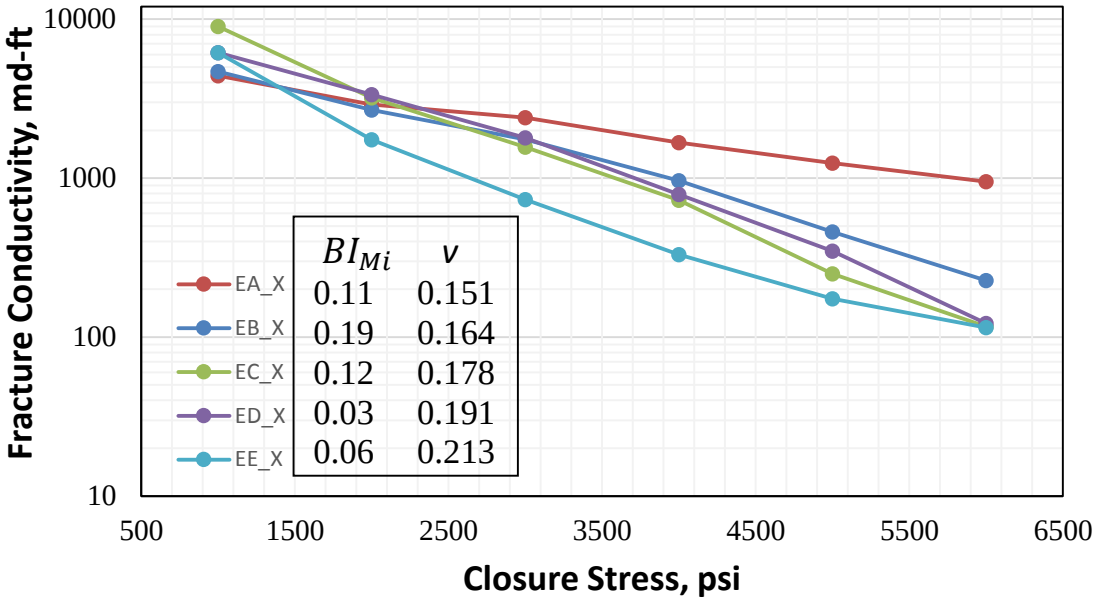

Fig. 4.5 – Fracture Conductivity Facies A-E and Brittleness Indexes. 30/50 Mesh- 0.1 lbm/ft^2 Concentration.

Table. 4.3 – Number of Data Points Used to Calculate the X0 and X90 Averages.

Facies	100	3050	Unpropped
EA_X	3	1	4
EB_X	7	4	4
EC_X	5	2	1
ED_X	4	2	3
EE_X	3	3	2

The same process was applied to obtain the average unpropped conductivity across the five geological facies (**Fig. 4.6**). In order to have more data points, the averages were calculated up to 1,000 psi of closure stress. Facies A and B (very similar conductivities) which have the highest conductivities are zones with high brittleness indexes, zones E and

D have lower conductivities than zones A and B and also have lower brittleness indexes. Facies C is the one with the lowest conductivity. It is important to note that only one successful unpropped conductivity experiment was performed in this zone, therefore, there is a possibility that this point is an outlier. Poisson's Ratio seems to be inversely related to fracture conductivity. However, the trend is not as clear as in the 100 mesh experiments.

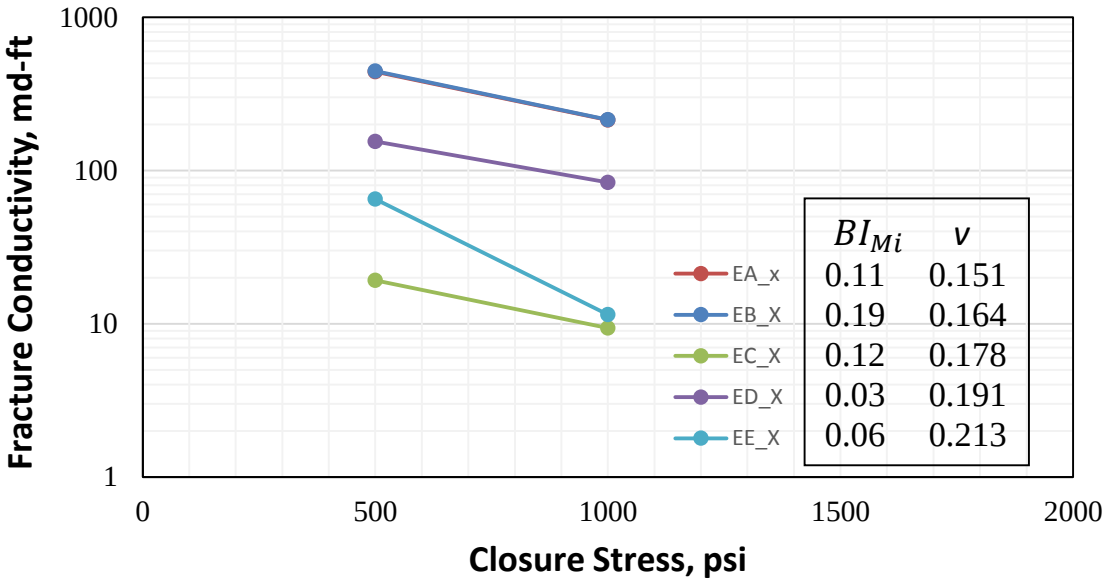

Fig. 4.6 – Fracture Conductivity Facies A-E and Brittleness Indexes-Unpropped.

5. CONCLUSIONS AND RECOMMENDATIONS

5.1 Conclusions

This work presents a comprehensive study on the fracture conductivity, propped and unpropped, of the five geological facies present in the Eagle Ford shale (Southwest Texas outcrops). First, the relationship between surface roughness (via mean root square method) and fracture area with fracture conductivity was analyzed for the five geological facies. Comparisons of the fracture conductivities across the five geological facies were made based on the mechanical properties and mineralogy of each facies. The conclusions of this work are summarized below:

(1) Propped and unpropped fracture conductivity declines exponentially with closure stress. For a concentration of 0.1 lbm/ft^2 the conductivity created with 30/50 mesh proppant is greater than the one created with 100 mesh proppant. However, the difference decreases as closure stress increases and at 6,000 psi both conductivities are almost equal. Propped conductivity is more than one order of magnitude higher than unpropped conductivity at low closure stress (less than 1,000 psi) and the difference increases as closure stress increases.

(2) For Facies A, B and C the surface attributes have a positive relationship with conductivity. In general, a high surface roughness (RMS) correlates to a high initial fracture conductivity and a high surface area correlates with high conductivities at high closure stresses. Facies D and E do not follow these trends. The mechanical

properties or heterogeneity may be dominating the conductivity of these facies, though we cannot affirm this with the available data.

(3) There is no obvious effect of fracture orientation between the X0 and X90 directions across the five geological facies. At low closure stresses in facies A, the conductivity of samples in the X0 direction is greater than the conductivity of samples in the X90 direction. The same can be said for facies D. Facies B, C and E show the opposite trend, where the conductivity in the X90 direction is greater than the one in the X0 direction. At high closure stress the conductivity in X0 and X90 have similar values for facies B, C and D. In facies A, there is a significant difference between the X0 (greater than) and X90 direction at high closure stress which may be caused by weak planes in the fracture face. Facies E shows a significant difference at low and high closure stresses between X0 and X90 (greater than). The conductivity in the Z direction seems to be smaller than the one obtained in the X0 and X90, however, only zone B was tested in this direction.

(4) Proppant dominates propped conductivity at low closure stress. As the closure stress increases there is a strong positive relationship between rock brittleness (calculated from the samples mineralogy) and fracture conductivity. Poisson's Ratio seems to be inversely related to fracture conductivity. From the brittleness indexes it is clear that there is a significant difference between facies E and D and the rest of the Eagle Ford shale.

5.2 Recommendations and Limitations

This work provides the upper limit of fracture conductivity for the samples used. It is a solid starting point but further studies are needed to fully understand and quantify the fracture conductivity of the Eagle Ford shale. The limitations of this study and recommendations to overcome them in future studies are presented below:

(1) All the experiments in this study were performed at dry conditions and at room temperature. The effect of formation temperature and water damage should be taken into consideration in order to improve the estimate of fracture conductivity.

(2) All the experiments were short term experiments, 30 minutes at each closure stress before measurements, long term experiments are needed in order to determine the effect of rock and proppant creeping on fracture conductivity.

(3) The mineralogy and mechanical properties on the fracture face of each sample should be determined in order to model the deformation on the fracture faces and the fracture width reduction.

(4) All the samples used in this studied were outcrops. Fracture conductivities on well cores should be obtained and compared to results from the outcrops in order to link these to the sub surface.

REFERENCES

Awoleke, O 2013. Dynamic Fracture Conductivity: An Experimental Investigation Based on Fractional Analysis. PhD dissertation, Texas A&M University, College Station, Texas (2013).

Barree, R.D. and Conway, M.W. 2009. Multiphase Non-Darcy Flow in Proppant Packs. *SPE Production & Operations*, 24(2): 257-268.

Brannon, H.D., Malone, M.R., Rickards, A.R., Wood, W.D., Edgeman, J.R., and Bryant, J.L. 2004. Maximizing Fracture Conductivity with Proppant Partial Monolayers: Theoretical Curiosity or Highly Productive Reality?. Paper SPE 90698 presented at the SPE Annual Technical Conference and Exhibition, Houston, Texas, U.S.A., 26-29 September.

Brannon, H.D., and Starks, T.R., 2008. The Impact of Effective Fracture Area and Conductivity on Fracture Deliverability and Stimulation Value. Paper SPE 116057 presented at the Annual Technical Conference and Exhibition, Denver, Colorado, U.S.A., 21-24 September.

Briggs, K. E. 2014. The Influence of Vertical Location on Hydraulic Fracture Conductivity in the Fayetteville Shale. M.S. Thesis, Texas A&M University, College Station, Texas (May 2014).

Cinco, L.H., Samaniego, F.V., and Dominguez, H.A. 1978. Transient Pressure Behavior for a Well with a Fine-Conducive Vertical Fracture. Paper SPE-6014-PA.

Cipolla, C.L., Lolon, E., Mayerhofer, M.J., and Warpinski, N.R. 2009. The Effect of Proppant Distribution and Un-Propped Fracture Conductivity on Well Performance in Unconventional Gas Reservoirs. Paper SPE 119368 presented at the SPE Hydraulic Fracturing Technology Conference, the Woodlands, Texas, U.S.A., 19-21 January.

Cooke Jr. C.E 1973. Conductivity of Fracture Proppants in Multiple Layers. *Journal of Petroleum Technology*, 25(9): 1101-1107.

Cooke Jr. C.E 1975. Effect of Fracturing Fluids on fracture Conductivity. *Journal of Petroleum Technology*, 27(10): 1273-1282.

Darin, S.R. and Huitt, J.L. 1959. Effect of a Partial Monolayer of Proppant Agent on Fracture Flow Capacity. Paper SPE 1291 presented at the Annual Fall Meeting, Dallas, Texas, U.S.A., 4-7 October.

Davies, D.R., and Kuiper, T.O.H 1988. Fracture Conductivity in Hydraulic Fracture Stimulation. *Journal of Petroleum Technology*, 40.5: 550-552.

Donovan, A.D., Staerker, T.S., Pramudito, A., Li, Weiguo., Corbett ,M.J., Lowery, C.M., Romero, A.M., and Gardner, R.D. 2012. The Eagle Ford Outcrops of West Texas: A Laboratory for understanding Heterogeinities Within Unconventional Mudstone Reservoirs. *CGAGS Journal, v.* 1(2012). P. 162-185.

EIA 2016. Energy Information Agency: Drilling Productivity Report, http://www.eia.gov/petroleum/drilling/#tabs-summary-2 (Accessed 17 January 2016).

Gardner, R,D., Pope, M,C., Wehner, M,P., and Donovan, A,D. 2013. Comparative Stratigraphy of the Eagle Ford Group Strata in Lozier Canyon and Antonio Creek, Terrel County, Texas. *CGAGS Journal, v.*2(2013), p 42-52.

Gadde, P,B., Liu, Y., Norman, J., Bonnecaze, R., and Sharma, M,N. 2004. Modeling Proppant Settling in Water-Fracs. Paper SPE 89875 presented at the SPE Annual Technical Conference and Exhibition, Houston, Texas, U.S.A, 26-29 September.

Guzek, J.J. 2014. Fracture Conductivity of the Eagle Ford Shale. M.S. Thesis, Texas A&M University, College Station, Texas (August 2014).

Gillard, M., Medvedev, O., Pena, A., Medvedev, A., Penacorada, F., D'Huteau, A. 2010. A New Approach to Generating Fracture Conductivity. Paper 135034 SPE. Presented at the Annual Technical Conference and Exhibition, Florence, Italy, 20-22 September.

Huitt, J.L., and McGlothlin, B.B. 1958. The Propping of Fractures in Formations Susceptible to Propping-Sand Embedment. Paper 58-115 API. Drilling and Production Practice, New York, New York, U.S.A, 1 January.

Jansen, T.A., 2014. The Effect of Rock Properties on Hydraulic Fracture Conductivity in the Eagle Ford and Fayetteville Shales. MS thesis, Texas A&M University, College Station, Texas (December 2014).

Kamali, A., and Pournik. 2015. Rough Surface Closure – A closer Look at Fracture Closure and Conductivity Decline. Paper ISRM_EUROCK-2015-117. Presented at the International Society of Rock Mechanics Regional Symposium, Salzburg, Austria, 7-10 October.

Kamenov, A.N 2013. The Effect of Proppant Size and Concentration on Hydraulic Fracture Conductivity in Shale Reservoirs. MS thesis, Texas A&M University, College Station, Texas (May 2013).

King, G.E. 2012. Hydraulic Fracturing 101: What Every Representative, Environmentalist, Regulator, Reporter, Investor, University Researcher, Neighbor, and Engineer Should Know About Hydraulic Fracturing Risk. *Journal of Petroleum Technology*, 64(04): 34-42.

Knorr, A, F. 2016. Briggs, K. E. 2014. The Effect of Mechanical Properties on Fracture Conductivity in the Eagle Ford . M.S. Thesis, Texas A&M University, College Station, Texas (May 2016).

Martin, R., Baihly, J.D., Malpani, R. et al. 2011. Understanding Production from Eagle Ford-Austin Chalk System. Paper SPE 145117 presented at the SPE Annual Technical Conference and Exhibition, Denver, Colorado, USA, 30 October-2 November.

McGinley, M.J 2015. The Effect of Fracture Orientation and Anisotropy on Hydraulic Fracture Conductivity in the Marcellus Shale. MS thesis, Texas A&M University, College Station, Texas (May 2015).

Miceli-Romero, A.A. 2014. Subsurface and outcrop organic geochemistry of the Eagle Ford shale (Cenomanian-Coniacian) in west, southwest, central, and east Texas. PhD. Dissertation, University of Oklahoma, Norman, Oklahoma.

Palisch, T., Duenckel, R., Bazan, L., Heidt, H.J., and Turk, G. 2007. Determining Realistic Fracture Conductivity and Understanding its Impact on Well Performance-Theory and Field Examples. Paper SPE 106301 presented at the SPE Hydraulic Fracturing Technology conference, College Station, Texas, U.S.A., 29-31 January.

Parker, M., Glasbergen, G., van Batenburg, D.W., Weaver, J.D., and Slabaugh, B.F. 2005. High-Porosity Fractures Yield High Conductivity. Paper SPE 96848 presented at the SPE Annual Technical Conference and Exhibition, Dallas, Texas, U.S.A., 9-12 October.

Peng, S., and Zhang, J.D. 2007. Engineering Geology for Underground Rocks. Berlin; New York; Springer, Pag.102.

Ramurthy, M., Barree, R.D., Kundert, D.P., Petre, E., and Mullen, M. 2011. Surface-Area vs Conductivity-Type Fracture Treatments in Shale Reservoirs. *SPE Production and Operations*, 26(4): 357-367.

Raysoni, N., and Weaver, J. 2012. Long-Term Proppant Performance. Paper SPE 150669. Presented at the SPE International Symposium and Exhibition on Formation Damage Control, Lafayette, Louisiana, U.S.A., 15-17 February.

RRC 2016a. Railroad Commission of Texas: Texas Barnett Shale Total Gas Production,http://www.rrc.state.tx.us/media/22204/barnettshale_totalnaturalgas_day.pdf (Accessed 17 January 2016).

RRC 2016b. Railroad Commission of Texas: Eagle Ford Shale Information. http://www.rrc.state.tx.us/oil-gas/major-oil-gas-formations/eagle-ford-shale/. (Accessed 26 January 2016).

Tian, Y., Ayers, W.B., and McCain, W.D., Jr. 2012. Regional Analysis of Stratigraphy, Reservoir Characteristics, and Fluid Phases in the Eagle Ford Shale, South Texas. Gulf Coast Association of Geological Societies Transactions 62: 471-483.

Tian, Y., Ayers, W.B., and McCain, W.D., Jr. 2013. The Eagle Ford Shale Play, South Texas: Regional Variations in Fluid Types, Hydrocarbon Production and Reservoir Properties. Paper IP TC 16808 presented at the International Petroleum Technology Conference, Beijing, China, 26-28 March.

Validyne Engineering 2016. Pressure Sensors DP 15. Retrieved from: http://validyne.com/product/DP15_Variable_Reluctance_Pressure_Sensor_Capable_of_Range_Changes#sthash.ZtKD6ANy.dpbs on June 21, 2016.

Wang, F.P., and Gale, J.F.W. 2009. Screening Criteria for Shale Gas Systems. *Gulf Coast Association of Geological Societies Transactions*. 59, 779-794.

Warpinski, N.R., Mayerhofer, M.J., Vincent, M.C., Cipolla, C.L., and Lolon, E.P 2009. Stimulating Unconventional Reservoirs: Maximizing Network Growth While Optimizing Fracture Conductivity. Paper SPE 114173 presented at the SPE Unconventional Reservoirs Conference, Keystone, Colorado, USA, 10-12 February.

Warpinski, N.R. 2009. Stress Amplification and Arch Dimensions in Proppant Beds Deposited by Waterfracs. *SPE Production & Operations*, 25(4): 461-471. SPE-119350-PA

Zheng, B., and Ellsworth, D. 2010. The Role of Chemical Compaction in the Evolution of Permeability and Strength in Granular Aggregates. Paper ARMA-10-454 American Rock Mechanics Association. Presented at the 44th U.S Rock Mechanics Symposium and 5th U.S-Canada Rock Mechanics Symposium. Salt Lake City, Utah, U.S.A., 27-30 June.

Zhang, J.. 2014. Creation and Impairment of Hydraulic Fracture Conductivity in Shale Formations. Ph.D. Dissertation, Texas A&M University, College Station, Texas (May 2014).